



AFRL-OSR-VA-TR-2014-0042

Fundamental Thermal and Mechanical Properties of Boride Ceramics

William G. Fahrenholtz and Greg E.
Hilmas
Missouri University of Science and
Technology
Materials Science and Engineering
Dept., 222 McNutt Hall
Rolla, MO 65409

28-02-2014

Final Report

<p>DISTRIBUTION A: Distribution approved for public release.</p>

Air Force Research Laboratory
AF Office Of Scientific Research (AFOSR)/RTB1
Arlington, Virginia 22203
Air Force Materiel Command

REPORT DOCUMENTATION PAGE					Form Approved OMB No. 0704-0188	
<p>The public reporting burden for this collection of information is estimated to average 1 hour per response, including the time for reviewing instructions, searching existing data sources, gathering and maintaining the data needed, and completing and reviewing the collection of information. Send comments regarding this burden estimate or any other aspect of this collection of information, including suggestions for reducing the burden, to Department of Defense, Washington Headquarters Services, Directorate for Information Operations and Reports (0704-0188), 1215 Jefferson Davis Highway, Suite 1204, Arlington, VA 22202-4302. Respondents should be aware that notwithstanding any other provision of law, no person shall be subject to any penalty for failing to comply with a collection of information if it does not display a currently valid OMB control number.</p> <p>PLEASE DO NOT RETURN YOUR FORM TO THE ABOVE ADDRESS.</p>						
1. REPORT DATE (DD-MM-YYYY) 28-02-2014		2. REPORT TYPE Final Report			3. DATES COVERED (From - To) Feb 2009 - Nov 2014	
4. TITLE AND SUBTITLE Fundamental Thermal and Mechanical Properties of Boride Ceramics				5a. CONTRACT NUMBER FA9550-09-1-0168		
				5b. GRANT NUMBER		
				5c. PROGRAM ELEMENT NUMBER		
6. AUTHOR(S) William G. Fahrenholtz and Greg E. Hilmas				5d. PROJECT NUMBER		
				5e. TASK NUMBER		
				5f. WORK UNIT NUMBER		
7. PERFORMING ORGANIZATION NAME(S) AND ADDRESS(ES) Missouri University of Science and Technology Materials Science and Engineering Dept., 222 McNutt Hall Rolla, MO 65409				8. PERFORMING ORGANIZATION REPORT NUMBER		
9. SPONSORING/MONITORING AGENCY NAME(S) AND ADDRESS(ES) Air Force Office of Scientific Research 875 N. Randolph Street, Suite 325 Arlington, VA 22203				10. SPONSOR/MONITOR'S ACRONYM(S) AFOSR/NA		
				11. SPONSOR/MONITOR'S REPORT NUMBER(S)		
12. DISTRIBUTION/AVAILABILITY STATEMENT DISTRIBUTION A: Distribution approved for public release.						
13. SUPPLEMENTARY NOTES						
14. ABSTRACT <p>The goal of the project was to investigate the fundamental factors that control the elevated temperature mechanical and thermal properties of ultra-high temperature diboride ceramics that are relevant to future Air Force needs related to hypersonic aviation and scramjet propulsion. The three main areas of research were: 1) structure-property relationships; 2) thermal properties; and 3) elevated temperature mechanical behavior of zirconium diboride and zirconium diboride-silicon carbide ceramics. Significant progress was made in each of the project areas.</p>						
15. SUBJECT TERMS <p>Ultra-high temperature ceramics, thermal properties, mechanical properties</p>						
16. SECURITY CLASSIFICATION OF:			17. LIMITATION OF ABSTRACT UU	18. NUMBER OF PAGES 57	19a. NAME OF RESPONSIBLE PERSON William Fahrenholtz	
a. REPORT U	b. ABSTRACT U	c. THIS PAGE U			19b. TELEPHONE NUMBER (Include area code) 573-341-6343	

Table of Contents

Executive Summary	3
Objectives	4
Status of the Effort	4
Accomplishments/New Findings	4
Structure-Property Relationships	4
Thermal Properties	16
Ultra-High Temperature Mechanical Properties	33
Personnel Supported	48
Publications and Presentations	48
Peer-Reviewed Journal Papers	48
Theses and Dissertations	49
Invited Presentations	49
Contributed Presentations	50
Interactions/Transitions	51
Awards	52
Appendix A: PhD Dissertation of Jeremy Watts	54
Appendix B: PhD Dissertation of Matthew Thompson	55
Appendix C: PhD Dissertation of Eric Neuman	56
Appendix D: MS thesis of Devon McClane	57

Executive Summary

This report describes research performed as part of the project “Fundamental Thermal and Mechanical Properties of Boride Ceramics” that was funded through the Aerospace Materials for Extreme Environments program at the Air Force Office of Scientific Research on contract number FA9550-09-1-0168. The report describes technical progress made during the course of the project as well as listing publications and presentations that were generated. In addition, appendices summarize four graduate thesis projects that were supported by this contract.

The goal of the project was to investigate the fundamental factors that control the elevated temperature mechanical and thermal properties of ultra-high temperature diboride ceramics that are relevant to future Air Force needs related to hypersonic aviation and scramjet propulsion. The three main areas of research that are described in this report are: 1) structure-property relationships; 2) thermal properties; and 3) elevated temperature mechanical behavior. Significant progress was made in each of the project areas.

Elucidation of structure-property relationships began by measuring the magnitude of thermal residual stresses in ZrB_2 -SiC ceramics. Neutron diffraction and Raman spectroscopy revealed that SiC particles in ZrB_2 matrices were under significant compressive stresses, up to ~ 900 MPa at room temperature. Likewise, the ZrB_2 matrix was in tension. Variable temperature measurements showed that thermal stresses relaxed above 1400°C . Knowledge of tensile stresses in the matrix confirmed that SiC particles were the strength-limiting flaws in ZrB_2 -SiC ceramics. In addition, SiC particles above ~ 11.5 μm in diameter led to the formation of microcracks in the ZrB_2 matrix. Overall, strengths in excess of 1 GPa were possible when the SiC particle size was below ~ 4 μm . Strengths decreased in proportion to the inverse square root of SiC particle size, consistent with analysis based on the Griffith criterion. However, above the microcracking threshold, strengths were ~ 400 MPa and were independent of SiC particle size.

Room temperature thermal conductivities ranging from about 30 W/m \cdot K to over 100 W/m \cdot K have been reported for diboride ceramics with little explanation for the variations. As part of the present project, impurities such as W were found to have a significance effect on thermal conductivity. Transition metals in the same family as Zr, namely Ti and Hf, had minimal effect on thermal conductivity, while others such as Nb, Ta, and W had an increasing impact based on their position on the periodic table. Transition metals and carbon were found to impact both the phonon and electron contributions to thermal conductivity at room temperature, but had a decreasing effect as temperatures approached 2000°C .

The final aspect of the project was investigating the elevated temperature mechanical properties of ZrB_2 and ZrB_2 -SiC. As part of the project, a new ultra-high temperature mechanical testing system was built. The system is capable at testing at temperatures up to $\sim 2600^\circ\text{C}$ in inert environments. The first series of tests using the new system examined the strength of ZrB_2 up to 2300°C , the first measurements reported in the open technical literature for diborides above 1600°C since 1970. The study revealed that ZrB_2 maintained a strength of more than 200 MPa at 2300°C . In addition, the strength of ZrB_2 -SiC was investigated up to 1600°C in air. As with room temperature strength, the strength of ZrB_2 -SiC was controlled by the SiC particle size up to about 1000°C . At 1200°C and above, oxidation damage produced the critical flaws in the material.

The primary results of this research are detailed in the technical publications that resulted from the thesis and dissertation research of the graduate students. A complete list of publications and abstracts of the student thesis and dissertation documents are included in this report.

Objectives

The project goal was to improve the understanding of the thermal properties and mechanical behavior from ambient to temperatures of 2000°C or higher. In the initial stage of the project, research focused on measuring thermal stresses in ZrB₂-SiC ceramics and measuring the thermal properties of dense ZrB₂ ceramics at elevated temperatures. In the latter stages of the project, the effort focused on measuring mechanical properties of ZrB₂ and ZrB₂-SiC at temperatures above 2000°C and studying the effect of transition metal additives on the thermal conductivity of ZrB₂.

Status of the Effort

This program began on February 1, 2009 and ended on November 30, 2013. Significant progress was made toward the research objectives. The program is expected to have lasting impacts in several areas related to ZrB₂ and ZrB₂-SiC ceramics. The main areas of technical progress highlighted in this report are: 1) structure-property relationships; 2) thermal properties; and 3) elevated temperature mechanical behavior.

During the course of the project, two students completed PhD dissertations. In addition, two other students, one MS and one PhD, conducted a substantial portion of their research and will complete graduate degrees within a few months of the end of the project. Details of each of the graduate student projects is provided in appendices that follow the body of this report.

Accomplishments/New Findings

This section describes the main accomplishments and findings from the project. The results are organized into three groups, structure-property relationships, thermal properties, and elevated temperature mechanical properties.

Structure-Property Relationships

The goals of these studies were to characterize the thermal stresses that developed in ZrB₂-SiC ceramics during cooling from the processing temperature and to use that knowledge to elucidate the effect of SiC particle size on mechanical behavior of ZrB₂-SiC ceramics.

The ZrB₂-SiC particulate composites used to measure thermal stresses were prepared by reactive processing to control the isotopic content of boron. One of the isotopes of boron, ¹⁰B, is a strong neutron absorber and its content was minimized in the ceramics for this study. Ceramics were prepared from ZrH₂ (Alfa Aesar, Grade Z-1038, Ward Hill, MA, USA), boron (Ceradyne Boron Products, Isotopic enriched ¹¹B metal, Quapaw, OK, USA) and SiC powders (H.C. Starck, Grade UF-25, Goslar, Germany). The SiC powder was α -SiC consisting primarily of the 6H polytype. An appropriate amount of each powder was used to produce a 70 vol% Zr¹¹B₂-30 vol% SiC composite. The powders were attrition milled using a fluoropolymer lined vessel, acetone as the liquid medium, and SiC milling media (4.7mm diameter SiC satellites, Union Process, Akron, OH, USA). The powders were attrition milled for 2 hours to reduce particle size and to intimately mix the powders to facilitate later reaction. Following attrition milling the slurry was rotary evaporated to remove the acetone and minimize preferential settling. At this stage, an effort was made to limit the exposure of the powder to air as both the ZrH₂ and ¹¹B powders are reactive with oxygen and moisture in the atmosphere. The newly formed surfaces

from milling serve to increase their reactivity further. Following solvent removal, the dried powder was passed through a 60 mesh sieve to facilitate uniform die filling for hot pressing. Composites were densified by hot pressing at 1900°C with 32 MPa applied pressure using a temperature ramp sequence reported in our previous research.

Stress measurements were performed by neutron diffraction and Raman spectroscopy. Neutron diffraction was performed using the time of flight (TOF) method on the Spectrometer for Materials Research at Temperature and Stress (SMARTS) in the Lujan neutron scattering center at Los Alamos National Laboratory. The 70 vol% Zr^{11}B_2 -30 vol% SiC composite specimen (4.2mm x 5.2 mm x 30mm) was positioned vertically in a graphite holder within a tungsten element furnace situated such that only the specimen was exposed to the neutron beam. The specimen was heated under vacuum ($\sim 1.3 \times 10^{-3}$ Pa) to a maximum temperature of 1750 °C at a rate of 20 °C/min. Neutron diffraction patterns were collected at regular temperature intervals ranging from room temperature to 1750 °C during both heating and cooling cycles. The temperature was allowed to equilibrate for 15 minutes prior to each measurement. Diffraction data were then collected for approximately one hour at each temperature. Microstructures examined before and after testing indicated that no changes in grain size or shape occurred during the extended heating. The same procedure was followed to measure both pure Zr^{11}B_2 and SiC powders, except that the powders were contained in a niobium crucible. Single peak fitting as well as whole pattern fitting were performed using the General Structure Analysis System (GSAS) software package³³. Raman measurements were made using a Raman spectrometer (Horiba LabRAM ARAMIS, Edison, NJ, USA) employing a 633 nm HeNe laser and a 1 μm spot size. Prior to collecting data, the instrument was calibrated using a silicon standard and the main silicon peak at 520.0 cm^{-1} . Raman patterns were acquired only from the SiC particles within the microstructure since ZrB_2 is not Raman active. Spectra were acquired from 25 individual SiC particles from the surface of the specimen.

The change in intensity of a diffracted peak as a function of temperature is governed by the Debye-Waller factor. The intensity should decrease as temperature increases due to increased thermal vibrations. This change is completely reversible and as the specimen is cooled the intensity should return to its original value. Deviation from this behavior is an indication that the quantity of the phase in question has been altered during the experiment; whether by reaction, oxidation, or some other means. Plotting intensity as a function of temperature for representative peaks from Zr^{11}B_2 and SiC, the (110) and (108) respectively, revealed that the change in intensity as a function of temperature was reversible (Figure 1). The slight difference in diffracted intensities ($\sim 4\%$) between heating and cooling of the SiC is consistent with the loss of a small amount of SiC from the surface of the specimen due to active oxidation. Based on the thickness of the SiC depleted layer, approximately 4.5 vol% of the SiC was lost.

Full pattern fitting was used to evaluate thermal residual stresses. To gauge the accuracy of the full pattern fitting, the available single peak fits were compared to their counterparts in the full pattern fitting. The SiC (006) d-spacing, located nominally at 2.5120 Å, obtained at room temperature from the full pattern fit was the same as that obtained by the single peak fit to within 0.0001 Å, which was at the resolution of this measurement. The Zr^{11}B_2 (110) d-spacing, located nominally at 1.5842 Å, was different by only 0.0004 Å. This close agreement between techniques indicated that the full pattern fitting was able to fit the individual peaks with the same precision as the single peak method.

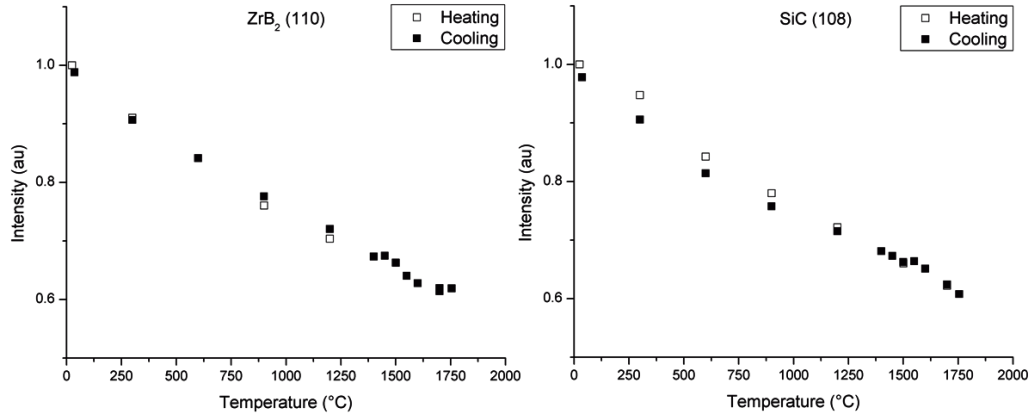


Figure 1. Neutron diffraction intensity as a function of temperature for representative Zr^{11}B_2 and SiC planes showing that the change in intensity between heating and cooling was negligible.

The residual stresses present in the Zr^{11}B_2 -SiC composites were calculated by comparing the lattice parameters of Zr^{11}B_2 and SiC from the composite with those of pure powders, which were assumed to be stress free. The strain (ϵ) in the composite was calculated by dividing the difference in lattice parameter (ΔL) between the composite and powder by the lattice parameter of the stress free powder (L_0), which was assumed to be unaltered by stress ($\epsilon = \Delta L / L_0$). By knowing the elastic modulus (E) of the material as a function lattice direction, the stress (σ) can then be calculated ($\sigma = E\epsilon$). Because the strains, and therefore the calculated stresses, are specific to a given crystallographic direction, the average elastic modulus of the material is not sufficient for the calculation of the directionally dependent stresses from the resolved stresses. Instead, the elastic modulus specific to each crystallographic direction must be used (E_{hkl}), which requires use of the full elastic matrix. Since ZrB_2 and α -SiC have hexagonal crystal structures, they each have five independent stiffness coefficients as shown in the elastic stiffness matrix (Equation 1). The values of each stiffness coefficient for both ZrB_2 and SiC are given in Table 1.

$$\begin{pmatrix} c_{11} & c_{12} & c_{13} & 0 & 0 & 0 \\ c_{12} & c_{11} & c_{13} & 0 & 0 & 0 \\ c_{13} & c_{13} & c_{33} & 0 & 0 & 0 \\ 0 & 0 & 0 & c_{44} & 0 & 0 \\ 0 & 0 & 0 & 0 & c_{44} & 0 \\ 0 & 0 & 0 & 0 & 0 & \frac{1}{2}(c_{11} - c_{12}) \end{pmatrix} \quad (1)$$

Table 1. The five independent stiffness coefficients for ZrB₂ and SiC

Material	c_{ij} (GPa)				
	c₁₁	c₁₂	c₁₃	c₃₃	c₄₄
ZrB ₂	567.8	26.9	120.5	436.1	247.5
SiC	511.7	112.6	53.3	565.2	167.6

Equation 2 was then used to relate the elastic constants to direction in the hexagonal crystal lattices to allow calculation of stresses from the strains measured by the diffraction method.

$$E_{hkl} = \frac{\left[h^2 + \frac{(h+2k)^2}{3} + \left(\frac{al}{c} \right)^2 \right]^2}{s_{11} \left(h^2 + \frac{(h+2k)^2}{3} \right)^2 + s_{33} \left(\frac{al}{c} \right)^4 + (2s_{13} + s_{44}) \left(h^2 + \frac{(h+2k)^2}{3} \right) \left(\frac{al}{c} \right)^2} \quad (2)$$

Using equation 2, the Miller indices of given directions for SiC and Zr¹¹B₂, and the compliance coefficients in Table 2, the elastic moduli were calculated for seven individual crystallographic directions for both SiC and Zr¹¹B₂ as shown in Table 3 and Table 4, respectively. Also in Table 3 and Table 4 are the stresses calculated for those crystallographic directions in both SiC and Zr¹¹B₂. These calculations predicted an average compressive stress within the SiC of ~880 MPa and a corresponding average tensile stress within the Zr¹¹B₂ of ~450 MPa for composites cooled to room temperature. In a composite such as this, the stresses within the two phases must be balanced. That is to say that using the rule of mixtures, the sum of the stresses, weighted according to volume fraction of each phase, must sum to zero, keeping in mind that tensile and compressive stresses are of opposite sign. Starting with the nominal SiC content of 30 vol% and the average measured compressive stress of 880 MPa, the tensile stress in the Zr¹¹B₂ would be expected to be ~380 MPa, which is only 70% of what was measured. However, the initial powders were attrition milled using SiC milling media. As a result, erosion of the media during milling added to the total amount of SiC within the composite. Performing areal analysis of SEM micrographs of the composite revealed that the SiC content comprised ~34 vol% of the composite and not 30 vol% as expected based on the starting powder composition. This analysis was based on the measurement of ~1000 SiC particles from 5 SEM images. Contamination from milling is common in ceramic processing, so SiC milling media were selected for this study to prevent the introduction of additional components into the system. Using 34 vol% SiC and its average compressive stress of 880 MPa, the tensile stress in the Zr¹¹B₂ was estimated to be ~450 MPa using the rule of mixtures calculation, which agrees with the neutron diffraction measurements that predicted an average tensile stress of ~450 MPa.

Table 2. The five independent compliance coefficients for ZrB₂ and SiC

Material	s_{ij} (GPa⁻¹)				
	s₁₁	s₁₂	s₁₃	s₃₃	s₄₄
ZrB ₂	1.88E-03	-8.28E-05	-4.95E-04	2.57E-03	4.04E-03
SiC	2.07E-03	-4.39E-04	-1.54E-04	1.80E-03	5.97E-03

Table 3. Elastic modulus, strain, and compressive stress in the SiC phase of a Zr^{11}B_2 -SiC composite for seven crystallographic directions

(h k l)	E_{hkl} (GPa)	ϵ	σ (MPa)
1 0 0	484	1.94E-03	937
1 0 1	474	1.94E-03	918
0 0 6	556	1.51E-03	842
1 0 2	452	1.93E-03	872
1 0 8	437	1.87E-03	820
1 1 0	484	1.94E-03	939
1 1 6	426	1.92E-03	815

Table 4. Elastic modulus, strain, and tensile stress in the Zr^{11}B_2 phase of a Zr^{11}B_2 -SiC composite for seven crystallographic directions

(h k l)	E_{hkl} (GPa)	ϵ	σ (MPa)
1 0 1	553	-9.00E-04	498
0 0 2	390	-7.18E-04	280
1 1 0	533	-1.01E-03	540
1 1 1	557	-9.61E-04	535
1 1 2	544	-8.80E-04	478
3 0 0	533	-1.01E-03	539
1 0 4	419	-7.45E-04	313

Neutron diffraction data was also analyzed to determine the temperature at which stresses began to accumulate during cooling. Figure 2 and Figure 3 are representative plots of the d-spacings as a function of temperature for SiC (Figure 2) and Zr^{11}B_2 (Figure 3) in the composite and as pure powders. The (006) planes of SiC in both the composite and powder had the same d-spacing at elevated temperature (Figure 2). Because diffusional mechanisms become active when temperatures are high enough to relax stresses, the composite should be stress free above some critical temperature. However, at 1200 °C and below, the d-spacings were no longer the same, indicating the development of strain in the SiC lattice and, therefore, residual stresses. Figure 3 illustrates the same behavior from the Zr^{11}B_2 (110) planes. At elevated temperature the lattice parameters of the powder and the composite were the same, but at 1200 °C and below they deviated. To estimate the temperature at which stresses began to accumulate, the powder d-spacing data were fitted with a second order polynomial. Likewise, the composite d-spacing data were fitted from 1200 °C and below to another second order polynomial. The fit to the composite d-spacing data was then extrapolated to higher temperatures until it intercepted the fit for the powder data. The two fit curves for both the SiC (006) and the Zr^{11}B_2 (110) intercepted one another at ~1400 °C. Similar analyses have been performed for other crystallographic planes in both SiC and Zr^{11}B_2 , all of which indicated that stresses begin to accumulate at ~1400 °C as the composite was cooled.

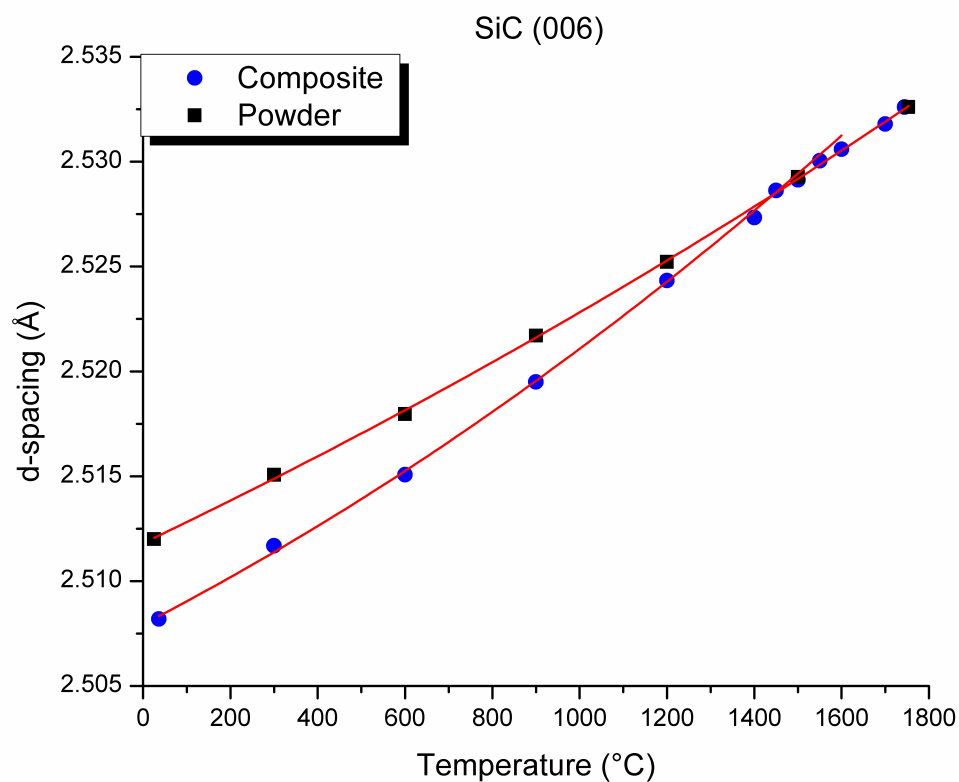


Figure 2. Measured d-spacing as a function of temperature for the SiC (006) peaks for both the composite and pure powder as measured by neutron diffraction along with their fitting curves.

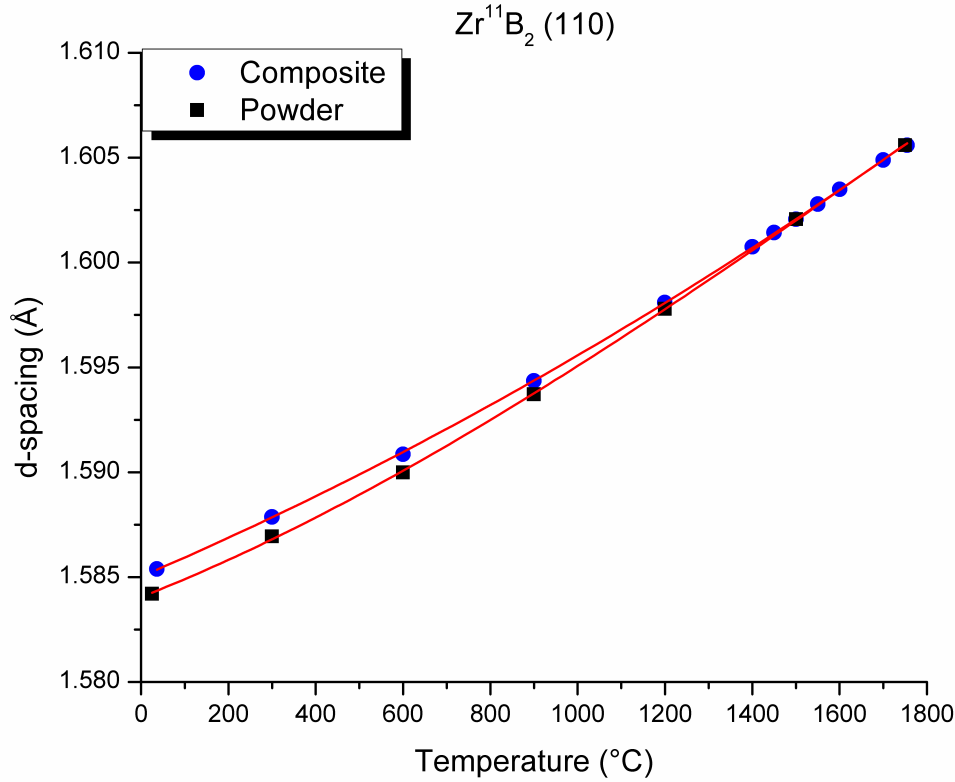


Figure 3. Measured d-spacing as a function of temperature for the $Zr_{11}B_2$ (110) peaks for both the composite and the powder as measured by neutron diffraction along with their fitting curves.

Stress measurement via neutron diffraction yielded an average stress over the entire sample due to the ability of the neutrons to penetrate through the specimens. Considering the specimen size, and its microstructure, on the order of billions of grains were sampled simultaneously during the neutron diffraction experiments. For comparison, Raman spectroscopy performed in this study utilized a small spot size ($\sim 1\mu m$) and therefore was expected to have only probed the top ~ 100 nm of the surface of the sample due to the laser wavelengths employed. As a result, Raman spectroscopy was able to probe the stresses in a single grain per measurement. Unfortunately, ZrB_2 is not Raman active; therefore stress measurements could only be performed on the SiC phase. Several peaks are associated with 6H SiC in Raman spectroscopy; the 2 main peaks are the transverse optic (TO) peak at 789.2 cm^{-1} and the linear optic (LO) peak at 970.1 cm^{-1} . These peak positions are sensitive to stress. While no general relationship has been determined to relate Raman peak shift to stress, researchers have measured peak shifts as a function of applied stress for a variety of materials including 6H SiC. Liu and Vohra measured the peak position of single crystals of 6H SiC as a function of applied pressure up to 95 GPa. By doing so they were able to develop a correlation between the position of the TO peak and stress (equation 3),

$$\omega_{TO}(\text{cm}^{-1}) = 790.2 + 3.11P - 0.009P^2 \quad (3)$$

where ω_{TO} is the measured peak position and P is the stress in GPa. In the present study, the position of the TO peak was measured from a Raman pattern from ~ 740 to 840 cm^{-1} and fitting the resultant peaks (Figure 4). Because of overlap between the TO peak and those surrounding it, the overall curve was deconvoluted to fit the individual peaks that comprise it. The central peak in Figure 4 is the TO peak, which was determined to be at 790.24 cm^{-1} . Inputting this value as ω_{TO} in equation 3 and solving for P results in a compressive stress of 335 MPa. While Figure 4 is representative of the Raman patterns, a range of stress values were measured. The average stress measured was 390 MPa; values ranged from 235 MPa to 595 MPa with a standard deviation of 100 MPa for 25 SiC grains measured to obtain these values. Assuming the cross section that was examined contained a random selection of SiC particles, some of the particles would be expected to be the top of larger particles that were predominantly below the surface. Others would be only the tips of particles that were almost completely removed by sectioning and polishing, while others would cover the range in between those two extremes. As a result, it is expected that the RAMAN peak shifts would provide a range of stresses when measuring individual particles as they were constrained differently depending on how much of each particle lay below the surface. The average stress of 390 MPa estimated from Raman peak shifts was only $\sim 44\%$ of the stress determined using neutron diffraction (880 MPa). Lower stresses can be expected from particles on the surface that were probed by Raman spectroscopy as compared to particles in the bulk that were probed by neutron diffraction. Modeling in Al_2O_3 -Al particle reinforced composites suggests that compressive stresses in particles on and near the surface are less than those of particles in the bulk due to decreased confinement by the matrix.

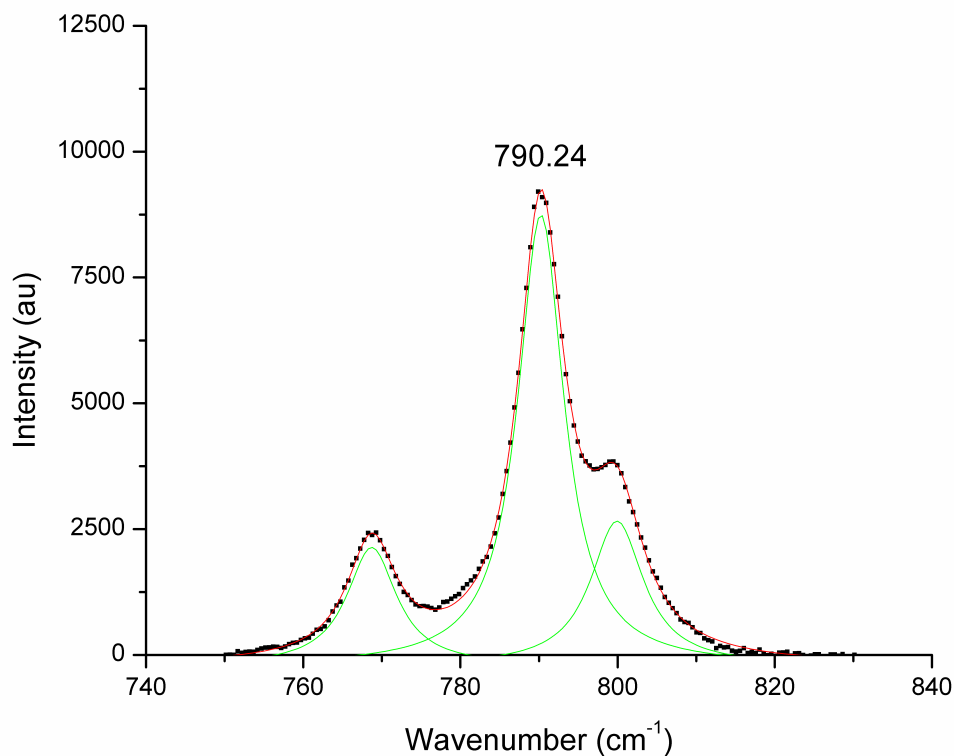


Figure 4. Raman pattern of a SiC grain within the Zr^{11}B_2 -SiC composite along with deconvoluted peak fits and peak position for the TO peak.

The deeper understanding of thermal residual stresses provided insight in to the room temperature mechanical behavior of ZrB₂-SiC ceramics. Four different sizes of SiC powders were used ranging from ~0.4 μm to ~11 μm . All of the composites in this study consisted of 70 vol% ZrB₂ and 30 vol% SiC. The compositions were produced by ball milling the SiC powder with ZrB₂ powder that had been attrition milled using WC media in acetone. The compositions designated as M1, M2, M4, and M8 in Table 5 were ball milled for 1, 2, 4, and 8 hours, respectively, to obtain a range of SiC particle sizes from the largest SiC powder. The composition designated as M0 was produced using the same powder without a ball milling step to avoid particle size reduction. The powders for this batch were mixed in acetone using both mechanical stirring, via a stir bar, as well as by suspending the beaker containing the powder-acetone suspension in an ultrasonic bath. The powders were mixed for a total of 3 hours and were placed in the ultrasonic bath for 1 minute after every 30 minutes of stir bar mixing. Following mixing, all powder batches were dried via rotary evaporation to minimize segregation during the drying process due to differential sedimentation. Following drying, the powders were passed through a 60 mesh sieve to facilitate die filling for hot pressing. Compositions were densified by hot pressing at 1900°C (2000°C for M0) and an applied load of 32 MPa.

Table 5. Composition designations and SiC powder used to produce ZrB₂-SiC composites

Composition Designation	SiC Powder Supplier	Grade	Starting SiC Particle Size (μm)		
			d10	d50	d90
UF-25	HC Starck	UF-25	0.17	0.37	0.69
UF-10	HC Starck	UF-10	0.31	0.70	1.49
UF-5	HC Starck	UF-5	0.56	1.87	4.65
M8, M4, M2, M1 and M0	Universal Photonics	Unasil 600 Green	7.08	11.06	16.40

Dense billets were machined into test bars (nominally 1.5 mm x 2 mm x 25 mm; ASTM C 1161-02b). Ten bars were machined from each composition for strength and modulus testing. The tensile surface of each specimen was polished to a 0.25 μm diamond finish. Strengths were measured using a semi-articulated fixture with a 20 mm lower span and 10 mm upper span in a screw driven instrumented load frame (Instron, 5881, Norwood, MA). Elastic modulus was determined using a deflectometer to measure the deflection of the center of the test bar during strength testing. Both Vickers and Knoop hardness were measured using a microhardness tester (Struers, Duramin 5, Cleveland, OH). Hardness was calculated from 10 indents per composition for both hardness techniques. Microstructural images were obtained using scanning electron microscopy (Hitachi, S570, Tokyo, Japan). Images of microcracking were also obtained using scanning electron microscopy (FEI, Helios Nano Lab 600, Eindhoven, The Netherlands). Final SiC particle sizes were measured by analyzing SEM images of each composition. Images containing ~500 SiC particles each were measured using image analysis software (Image J, National Institutes of Health, Bethesda, MD). The SiC particles were fit using an ellipse, and the major axis of that ellipse was used as the final maximum SiC particle size.

The flexure strength, elastic modulus, and both Vickers' and Knoop hardness were measured for ZrB₂-SiC composites with a range of SiC particle sizes (Table 6). Strength decreased as the SiC particle size increased. The highest strength was exhibited by the composition that had the smallest maximum SiC particle size of 4.4 μm and a strength of 1150

MPa. Both the elastic modulus and hardness values were nearly constant for compositions that had maximum SiC particle sizes of 11.5 μm and smaller. Composites containing SiC particles larger than 11.5 μm , however, exhibited an abrupt decrease in the measured values for strength, modulus, and hardness. The trends of the mechanical properties, as well as the abrupt change in behavior for SiC particle sizes greater than 11.5 μm , will be discussed in more detail below.

Table 6. Summary of mechanical properties for varying SiC particle size ZrB₂-SiC composites

Composition	Final Maximum SiC Particle size (μm)	Strength (MPa)	Elastic Modulus (GPa)	Vickers Hardness (GPa)	Knoop Hardness (GPa)
UF-25	4.4	1150 +/- 115	541 +/- 22	21.38 +/- 0.61	17.16 +/- 0.22
UF-10	6.4	924 +/- 100	532 +/- 13	21.73 +/- 0.64	17.06 +/- 0.30
UF-5	8.2	892 +/- 120	534 +/- 20	21.20 +/- 0.38	17.01 +/- 0.21
M8	11.5	825 +/- 118	531 +/- 14	21.24 +/- 0.55	17.12 +/- 0.27
M4	11.8	724 +/- 83	520 +/- 12	19.27 +/- 1.78	16.12 +/- 0.27
M2	12.0	460 +/- 47	518 +/- 16	18.64 +/- 0.54	15.58 +/- 0.37
M1	13.0	280 +/- 34	505 +/- 7	18.35 +/- 1.26	15.57 +/- 0.42
M0	18.0	245 +/- 23	484 +/- 6	17.28 +/- 1.42	15.23 +/- 0.29

Unlike previous studies that had shown a linear trend between average SiC particle size and strength of ZrB₂-SiC, the present study examined a wider range of SiC particle sizes. The larger range of particle sizes revealed that strengths followed a trend related to the maximum SiC particle size as described by the Griffith equation for flaw sizes of brittle materials (Equation 4).

$$\sigma_f = \frac{K_{IC}}{Y\sqrt{c}} \quad (4)$$

where σ_f is the failure stress, K_{IC} is the fracture toughness, Y is a geometric constant related to the fracture origin, and c is the critical flaw size of the material. Further, the aspect ratio of the SiC phase in the composites changed as a function of particle size, which complicated the analysis. The aspect ratio decreased from a maximum of 1.90 for the smallest SiC particle size sample to 1.45 for the largest SiC particle size. As a result, the use of equivalent circular diameter is not adequate to describe the SiC particle size. As the aspect ratio increases, a larger particle cross section may be subjected to the applied stress even though the overall area of the particle does not change. Following this observation, the SiC particle sizes were then fit using an ellipse instead of a circle, which allowed for the aspect ratio of the ellipse to change along with the aspect ratio of the SiC particles. From this analysis, the major axis of the ellipse was used as a more representative measure of the largest SiC cross section that could be exposed to stress during flexure testing. As the maximum SiC particle size increased from 4.4 μm to 11.5 μm the relationship between strength and particle size was consistent with trends predicted using the Griffith equation (Figure 5). That is to say, the strength changed in proportion to the square root of maximum SiC particle size as predicted by equation 4 when the maximum size was determined using the major axis of an ellipse. Above 11.5 μm , the strength decreased abruptly from 825 MPa to approximately 250 MPa. This type of behavior indicated a microstructural change within the composites. If the decrease in strength were merely due to the increase in SiC particle size, the change in strength would be expected to be continuous as a function of maximum SiC particle size.

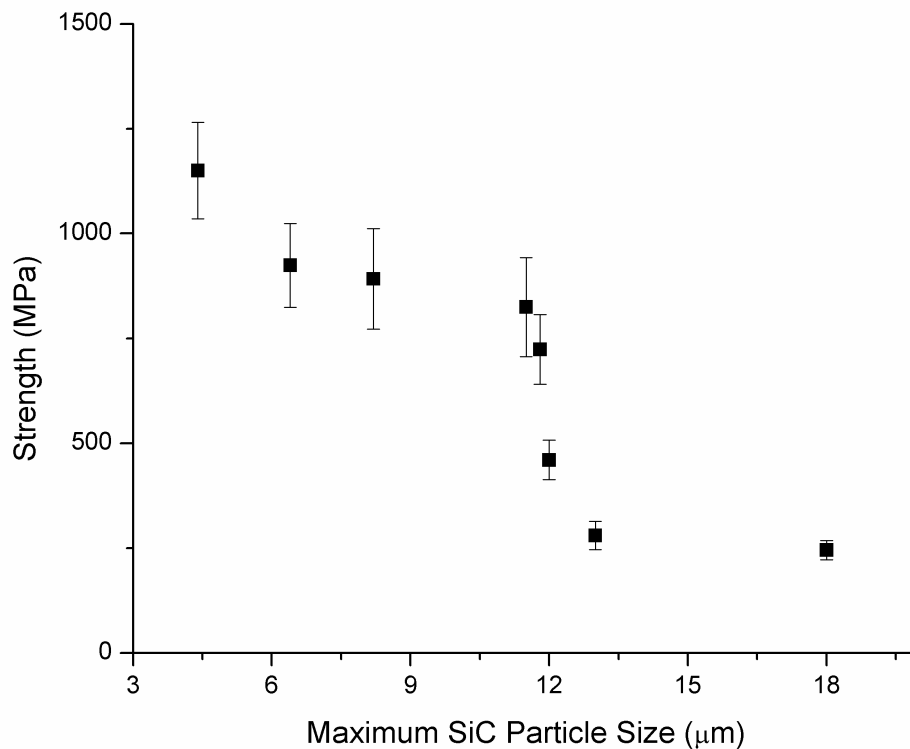


Figure 5. Strength as a function of maximum SiC particle size measured as the major axis of an ellipse for ZrB₂-SiC composites showing a $1/c^{1/2}$ relationship up to 11.5 μm at which point strength decreased more rapidly.

One likely cause of an abrupt change in strength is microcracking, which has been shown to cause similar decreases in the measured strength in other ceramic materials. The distribution in measured strength values, for the larger SiC particle size composites, was also consistent with what is expected from microcracked materials. For SiC particle sizes greater than 11.5 μm, the distribution of strengths was smaller. As shown in Table 6, the average distribution of strengths for compositions with SiC particle sizes of 11.5 μm and smaller was ± 113 MPa whereas the average strength distribution for larger particle sizes was less than half that of smaller average SiC particle sizes at ± 47 MPa. As the microcracks began to grow, the strengths became more uniform as the failure origins became a more consistent size.

To further investigate whether or not microcracks were the cause of the decrease in strength for composites containing SiC particles greater than 11.5 μm in size, both the elastic modulus and hardness were examined. The elastic modulus values measured for the ZrB₂-SiC composites followed the same pattern as the strengths. For SiC particle sizes of 11.5 μm and smaller, the elastic modulus remained constant at ~ 530 GPa. In contrast, for composites with larger SiC particle sizes the modulus was markedly reduced to ~ 480 GPa (Figure 6). A change in SiC particle size alone, without some other microstructural change, would not change the elastic modulus of the composite since the volume fraction of each phase did not change. Figure 6, however, clearly illustrates a decrease in the elastic modulus for composites with maximum SiC particle sizes larger than 11.5 μm. The M0 material had an elastic modulus of 484 GPa,

which was a decrease of ~10% compared to those of the UF-25, UF-10, UF-5, and M8 compositions. A threshold at which elastic modulus decreased was consistent with what has previously been observed for a material that begins to exhibit microcracking at some critical particle size. Monolithic oxide ceramics have been shown to exhibit decreases in elastic modulus of as much as 70% once the critical grain size for microcracking has been exceeded. Likewise, these $\text{ZrB}_2\text{-SiC}$ ceramics also exhibited significant decreases in microhardness when the maximum SiC particle size reached $11.5\text{ }\mu\text{m}$, further supporting the conclusion that microcracks led to the decrease in strength. Finally, the presence of microcracks was confirmed using high resolution electron microscopy (Figure 7). No microcracks were observed in $\text{ZrB}_2\text{-SiC}$ composites with smaller SiC particle sizes.

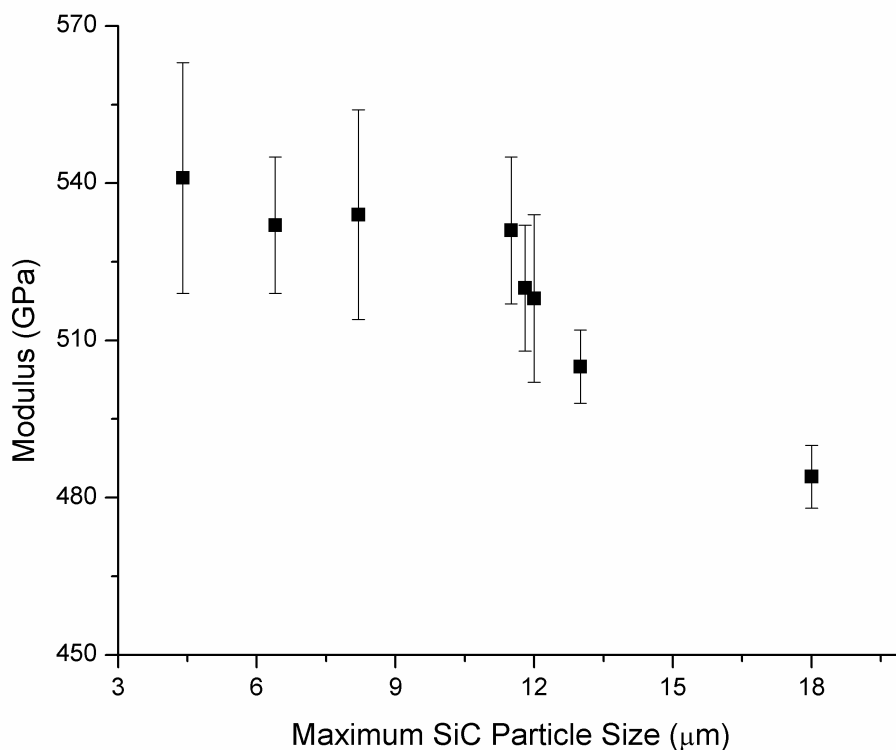


Figure 6. Elastic modulus as a function of the maximum SiC particle size measured as the major axis of an ellipse showing a reduction in modulus for composites containing SiC particles larger than $11.5\text{ }\mu\text{m}$.

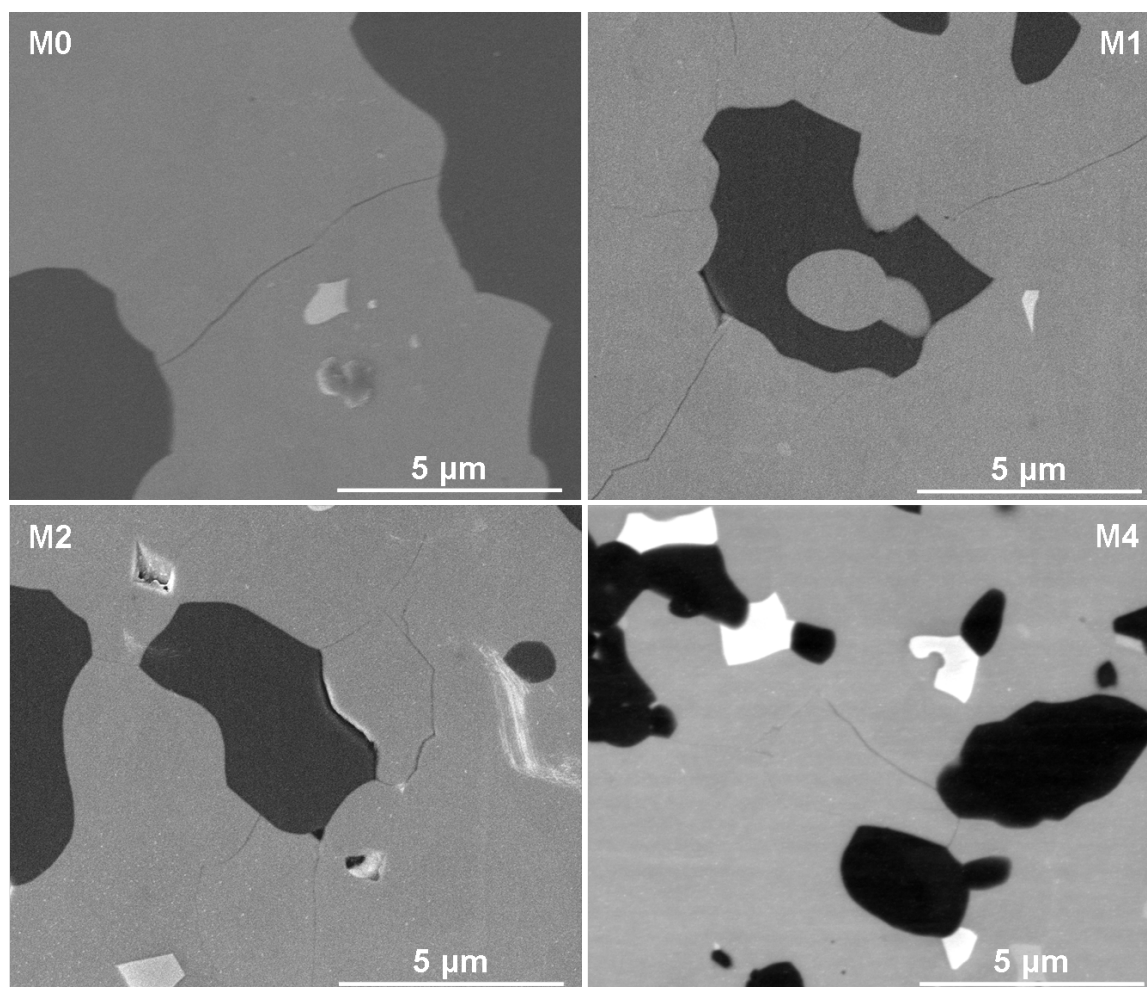


Figure 7. SEM micrographs of the M0, M1, M2, and M4 compositions indicating microcracking of the ZrB_2 matrix phase.

Thermal Properties

The effect of carbon additions on the thermal conductivity of ZrB_2 was studied. Commercially available ZrB_2 powder was attrition milled in hexane for two hours using Co-bonded WC milling media in a fluoropolymer lined bucket. The resulting slurry was rotary evaporated to remove hexane. Milling reduced the average particle size of the ZrB_2 from $\sim 2\ \mu\text{m}$ to $\sim 0.2\ \mu\text{m}$, which was measured by laser light scattering. The mass of the WC milling media was measured before and after milling, which indicated that $\sim 2\ \text{wt}\%$ WC was incorporated into the ZrB_2 powder. The oxygen content after attrition milling was 2.06 wt%. Carbon was added as phenolic resin (GP 2074, Georgia Pacific, Atlanta, GA) that was dissolved in acetone. The phenolic resin solution was added to a slurry of ZrB_2 particles in acetone. The resulting mixture was then rotary evaporated to remove the acetone, which left the ZrB_2 particles coated with phenolic resin. The resulting powder was heated at $10^\circ\text{C}/\text{min}$ to 700°C and held for 2 hours in flowing Ar to convert the phenolic resin to amorphous carbon. The carbon yield of the phenolic resin was 41 wt%. Powders were densified by hot pressing. Hot pressed specimens were surface ground and cut into squares approximately 12.5 mm by 12.5 mm by 3 mm thick. The outer portions of the billets were ground or cut away to remove the portion of the pellet that may have

been affected by reaction with the hot press die. The bulk density of each specimen was measured by the Archimedes' technique using vacuum infiltration with distilled water as the immersing medium. Specimens were polished using successively finer diamond abrasives with a final abrasive size of 0.25 μm . Carbon inclusions that were visible on the polished surfaces were analyzed using Raman spectroscopy with a 633 nm HeNe laser and a 1 μm spot size. Thermal diffusivity was measured by the laser flash technique following the procedure defined in ASTM standard E1461. Specimens were coated with graphite and then analyzed up to 2000°C in flowing Ar that was maintained at a gauge pressure of ~41 kPa. Each data point was an average of 3 tests taken every 2 minutes after the specimen had been held at a constant temperature for 7 minutes. Results were calculated using the Clark and Taylor method for determining thermal diffusivity according to Equation 5. In this calculation, thermal diffusivity (α) was dependant on specimen thickness (L) and time for the specimen to rise to half of the maximum temperature ($t_{1/2}$) after the laser pulse. Thermal conductivity (λ) was then calculated at each temperature from the measured thermal diffusivity (α), heat capacity (C_p) from the NIST-JANAF tables, and bulk density (ρ) using Equation 6.

$$\alpha = \frac{0.1388L^2}{t_{1/2}} \quad (5)$$

$$\lambda = \alpha \rho C_p \quad (6)$$

Electrical resistivity was measured as a function of temperature up to 1200°C in flowing Ar. Measurements were made by the 4-point van der Pauw method (ASTM standard F76) on 12.5 mm round disks that had a thickness of 0.5 mm. Data were collected during cooling after equilibrating for 10 minutes at each test temperature. Nickel electrodes were used for the measurements and they were joined to the specimens with platinum paint. Equation 7 was then used to calculate electrical resistivity based on specimen thickness t , maximum current I , voltages in given directions $V_{ij,kl}$, and a geometric factor f that was dependent on the voltages. The reciprocal of electrical resistivity, electrical conductivity, was then used for discussion.

$$\rho = \frac{1.1331ft}{I} [V_{21,31} - V_{12,34} + V_{32,41} - V_{23,41}] \quad (7)$$

Zirconium diboride (ZrB_2) was densified with carbon additions up to 3 wt%. As summarized in Table 7, adding carbon decreased the time required for densification at 1900°C. The specimen with no intentionally added carbon (designated AM0C to indicate attrition milled powder with 0 wt% carbon addition) required ~35 min at 1900°C to reach nearly full density. In contrast, only ~10 min at 1900°C was required to densify the specimens with 1 wt% (AM1C) and 3 wt% (AM3C) carbon added. Carbon additions also led to a decrease in the final oxygen content of the hot pressed ZrB_2 . Oxygen was likely removed by a combination of evaporation of B_2O_3 and carbothermal reduction of ZrO_2 and B_2O_3 . The final oxygen content in the ceramic with no carbon addition (AM0C) was 0.40 wt% compared to an oxygen content of ~2.06 wt% for the powder prior to hot pressing. Presumably, the reduction in oxygen content from 2.06 wt% to 0.40 wt% was mainly due to B_2O_3 evaporation. In contrast, the final oxygen contents for the ceramics with carbon additions (AM1C and AM3C) were ≤ 0.05 wt% due to removal of oxygen by carbothermal reduction in addition to B_2O_3 evaporation. This behavior showed that carbon additions not only reduced the final oxygen content of the ceramics but also decreased the bulk density because of excess carbon present in the microstructure.

Table 7. Summary of processing conditions and properties of hot pressed ZrB₂ ceramics.

Designation	Carbon added (wt%)	Final oxygen content (wt%)	Time at 1900°C (min)	Bulk Density (g/cm ³)	Grain size (μm)	Observed carbon (vol%)
AM0C	0	0.40	35.0	6.22	3.3 ± 2.2	0
AM1C	1	0.05	10.0	6.19	2.4 ± 1.3	1.4
AM3C	3	0.03	12.5	6.01	1.8 ± 0.9	10.8

Carbon additions led to a noticeable decrease in grain size in the dense ceramics (Figure 8Figure 1). For AM0C and AM1C, no second phases were visible in polished, thermally etched cross sections. The grain size was 3.3 μm for AM0C after densification, but it decreased to 2.4 μm for AM1C, presumably due to the decreased time required for densification. In contrast to ceramics with 0 or 1 wt% carbon, the addition of 3 wt% carbon produced a distinct second phase. The densification time for AM3C was about the same as AM1C, but the presence of carbon inclusions pinned grains, which further reduced the average grain size of the resulting ZrB₂ to 1.8 μm. The addition of 3 wt% carbon resulted in the presence of ~10 vol% carbon in the final ceramic, which was particularly visible in polished sections (not shown). Based on SEM observations, the ceramic with 1 wt% carbon added appeared to be below the solid solubility limit for carbon in ZrB₂, which resulted in a majority of the carbon dissolving into the ZrB₂ matrix during densification. In contrast, the addition of 3 wt% carbon was above the solid solubility limit, which resulted in the presence of visible carbon inclusions. Overall, carbon additions reduced the grain size of ZrB₂ by reducing grain coarsening due to shorter times required for densification for both levels of carbon addition and grain pinning with carbon additions that produce a second phase.

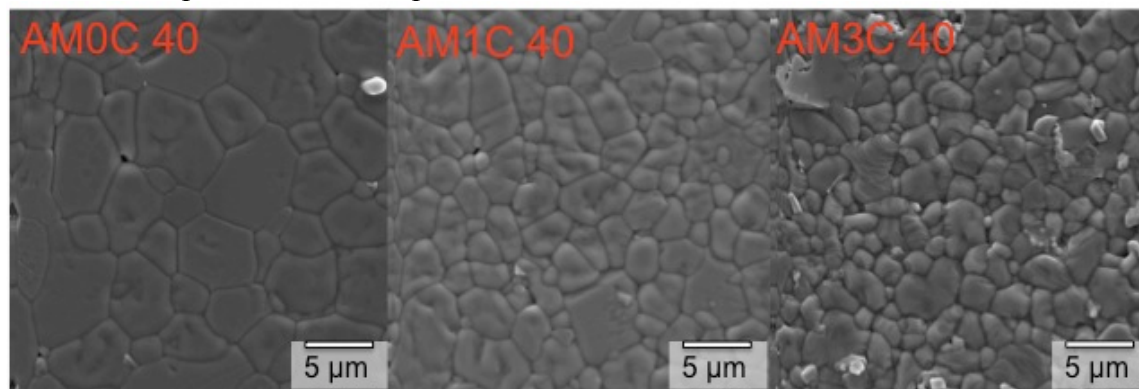


Figure 8. SEM images of AM0C, AM1C, and AM3C. These specimens were sectioned perpendicular to the hot pressing direction, polished, and then thermally etched to highlight the grain boundaries.

Thermal diffusivity was measured as a function of carbon content from 200°C to 2000°C. For each material, the thermal diffusivity had a maximum value at 200°C and decreased to a minimum value at 2000°C (Figure 9). For example, the maximum thermal diffusivity for AM3C was 0.176 cm²/sec at 200°C and it decreased to a minimum value of 0.143 cm²/sec at 2000°C. Without added carbon, the thermal diffusivity decreased from a maximum of 0.149 cm²/sec at 200°C to a minimum value of 0.129 cm²/sec at 2000°C. Regardless of the carbon addition, the

thermal diffusivity decreased up to 2000°C because of increased phonon scattering with increased temperature. Among the three materials measured in the present study, AM3C had the highest thermal diffusivity at 200°C with a value of 0.176 cm²/sec compared to 0.149 cm²/sec for AM0C. In contrast, AM1C had the lowest value of 0.129 cm²/sec at 200°C. The dissolved carbon present in AM1C reduced its thermal diffusivity compared to AM0C because of a reduction in phonon transfer processes by forming a solid solution. In contrast, the presence of carbon as a second phase in AM3C increased its thermal diffusivity at 200°C to 0.176 cm²/sec. The additional carbon phase in AM3C may have increased the thermal diffusivity of the ceramic due to the higher thermal diffusivity of graphite (0.53 cm²/sec at 25°C) compared to ZrB₂.

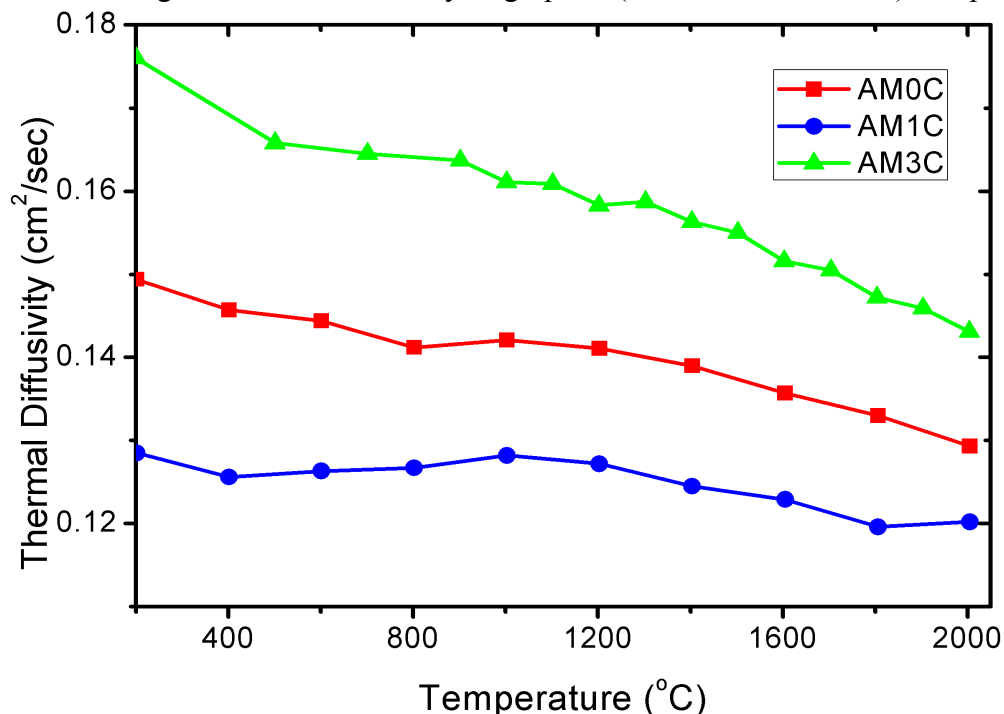


Figure 9. Thermal diffusivity as a function of temperature measured during cooling from 2000°C for ZrB₂ ceramics with three different carbon contents.

For ZrB₂ with carbon additions, the thermal diffusivity of the as processed specimens did not follow the same path upon heating and cooling during the first thermal cycle. The largest differences were noted in AM3C (Figure 10). The first diffusivity run started with a value of 0.118 cm²/sec measured at 1000°C and increased up to 0.140 cm²/sec at 2000°C. Upon cooling, the diffusivity increased further to 0.160 cm²/sec at 1000°C. However, this initial measurement (i.e., heating the as-processed specimen to 2000°C) stabilized the value of thermal diffusivity so that the values measured in all subsequent runs followed the cooling path of the first run during both heating and cooling. Therefore, the second run (and all subsequent runs) for composition AM3C started at 0.160 cm²/sec at 1000°C and decreased to 0.143 cm²/sec at 2000°C. On cooling, the diffusivity followed the same path as heating, resulting in a diffusivity of 0.165 cm²/sec at 800°C. Based on SEM analysis, the increase in thermal diffusivity observed during the initial heating cycle was due to changes in the microstructure that did not affect the measured heat capacity values, which were the formation of ZrC and grain growth.

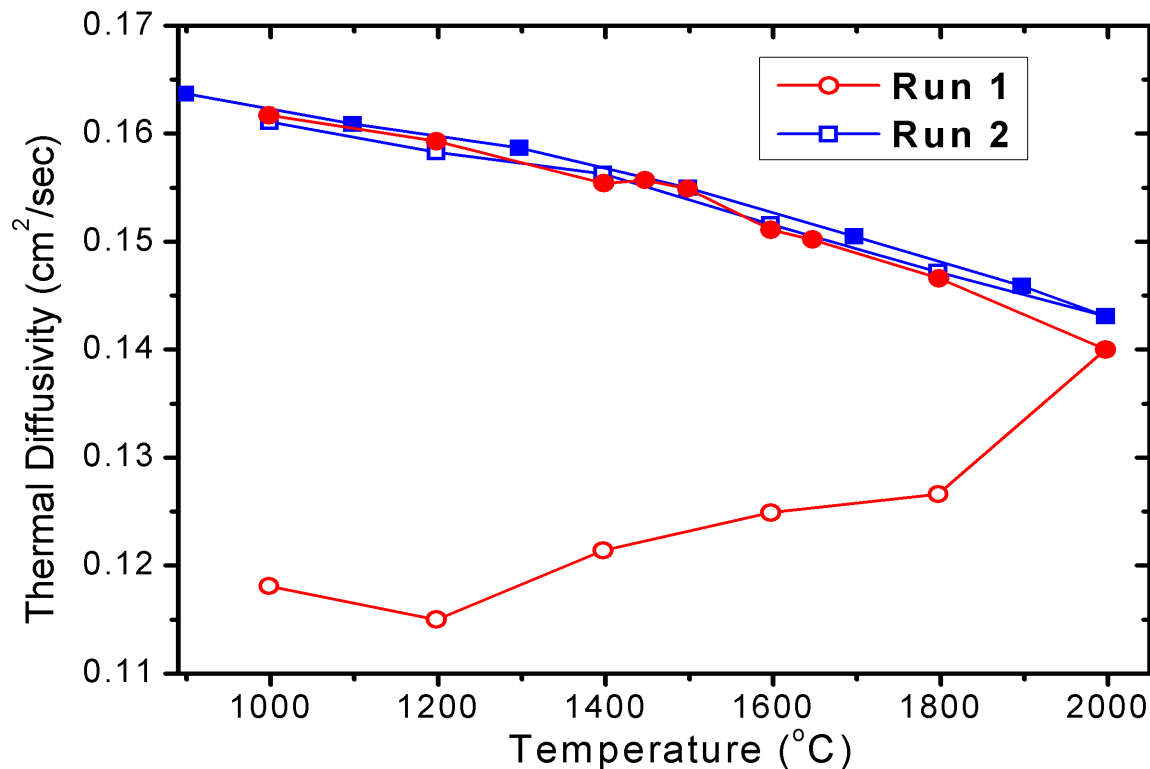


Figure 10. Thermal diffusivity as a function of temperature during heating (open symbols) and cooling (filled symbols) of AM3C for its first diffusivity run (circles) and a second run (squares).

Quantitative x-ray diffraction confirmed that after cycling to 2000°C AM3C contained approximately 97.1 wt% ZrB₂ and 2.9 wt% ZrC. In addition, the observed ZrC peaks were shifted to higher 2θ values than those from the powder diffraction file card for pure ZrC (PDF card number 35-0784). The shift to higher 2θ values corresponds to a decrease in the ZrC lattice parameter from 4.691 Å reported for pure ZrC to 4.653 Å. The decrease suggests that some of the W that was introduced into the material as an impurity from the WC media used in the attrition milling process migrated into the ZrC that formed during thermal cycling. The total WC impurity content of the ceramics was ~2.2 wt% based on mass loss from the media. After hot pressing, WC appeared to be dissolved in the ZrB₂ matrix since no WC inclusions were observed by SEM and no WC peaks were detected by XRD and no other phases were observed by SEM. After heating to 2000°C, analysis of the lattice parameter of the ZrC showed that the ZrC grains contained ~15 wt.% W, which was equivalent to 0.45 wt% W based on a total system composition of 2.2 wt% WC. Thus, even though ZrC made up only 2.67 vol% (2.9 wt%) of the specimen, it contained about 20% of the total W.

Thermal conductivity, shown in Figure 11, increased with increasing temperature for each composition, reaching a maximum value at 2000°C. Thermal conductivity was highest for AM3C and lowest for AM1C while values for AM0C were between the other two materials. For example, the highest thermal conductivity at 2000°C was 64.2 W/m•K for AM3C compared to 58.7 W/m•K for AM0C. The addition of 1 wt% carbon led to a decrease in grain size and, presumably, the dissolution of carbon into the ZrB₂, which decreased the thermal conductivity to 53.9 W/m•K at 2000°C. The addition of 3 wt% carbon led to the formation of carbon as a

second phase, but also produced ZrC during the first thermal cycle after processing. The increase in thermal conductivity of AM3C after heating to 2000°C relative to the other two materials was due to the presence of carbon, the formation of ZrC, and the migration of W from the ZrB₂ into the ZrC.

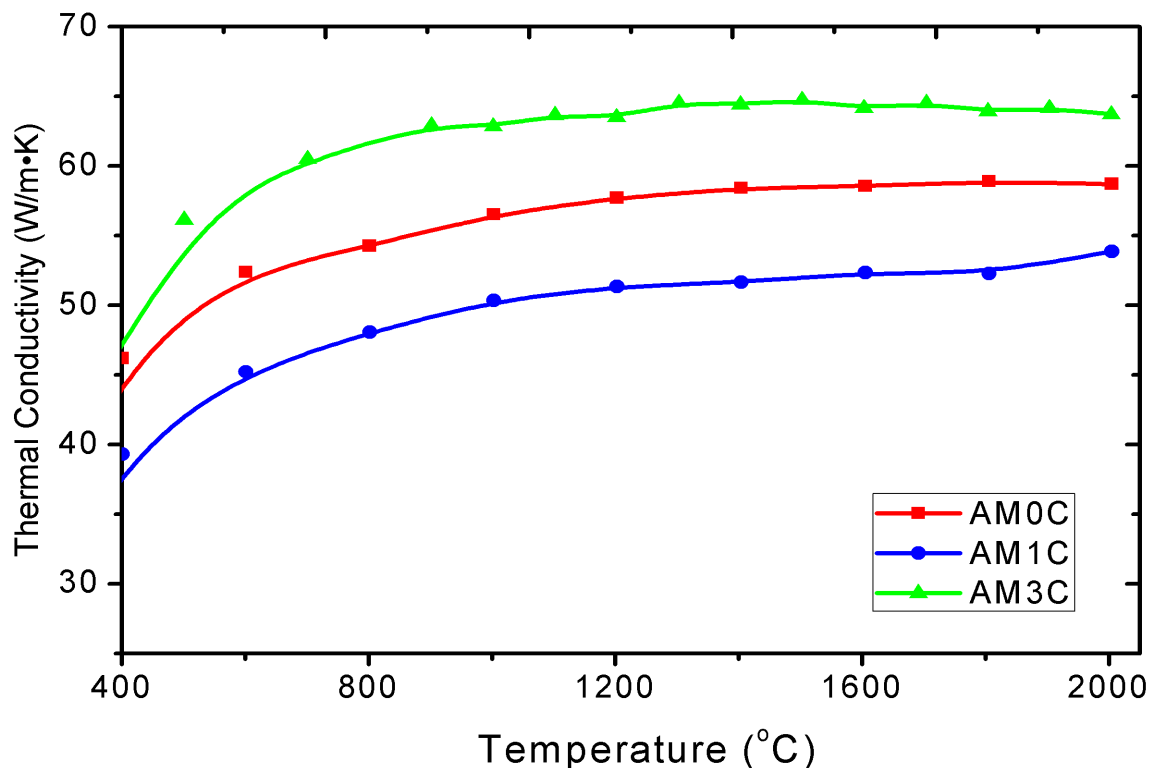


Figure 11. Thermal conductivity as a function of temperature for AM0C, AM1C, and AM3C calculated from measured heat capacity and thermal diffusivity.

To better understand the distribution of carbon in the three ZrB₂-based ceramics, STEM imaging was used (Figure 12). For AM0C, traces of carbon were observed along the grain boundaries while image analysis revealed ~1.4 vol% in AM1C. Carbon was considered to be an isolated, trace phase in both of these materials, although AM1C was expected have a significant amount of carbon dissolved into the ZrB₂ matrix since 1 wt% was added. In contrast, the addition of 3 wt% carbon led to the presence of 10.8 vol% carbon in AM3C, which was present both as carbon dissolved into the ZrB₂ matrix and as carbon inclusions. The carbon inclusions in AM3C also had a pronounced aspect ratio, estimated to be ~12 using image analysis software. Previous work by Garboczi et al. with percolation theory showed that with an aspect ratio of 12, the percolation threshold is 7.8 vol% in a polycrystalline matrix. Therefore, the carbon observed in AM3C could be above the percolation threshold.⁴² Therefore, the carbon inclusions were likely to form a network having random, 3D connectivity. Further, the connected carbon network could be responsible for part, if not all, of the increase in thermal conductivity of AM3C relative to AM0C because graphite has a higher thermal conductivity than the ZrB₂ matrix.

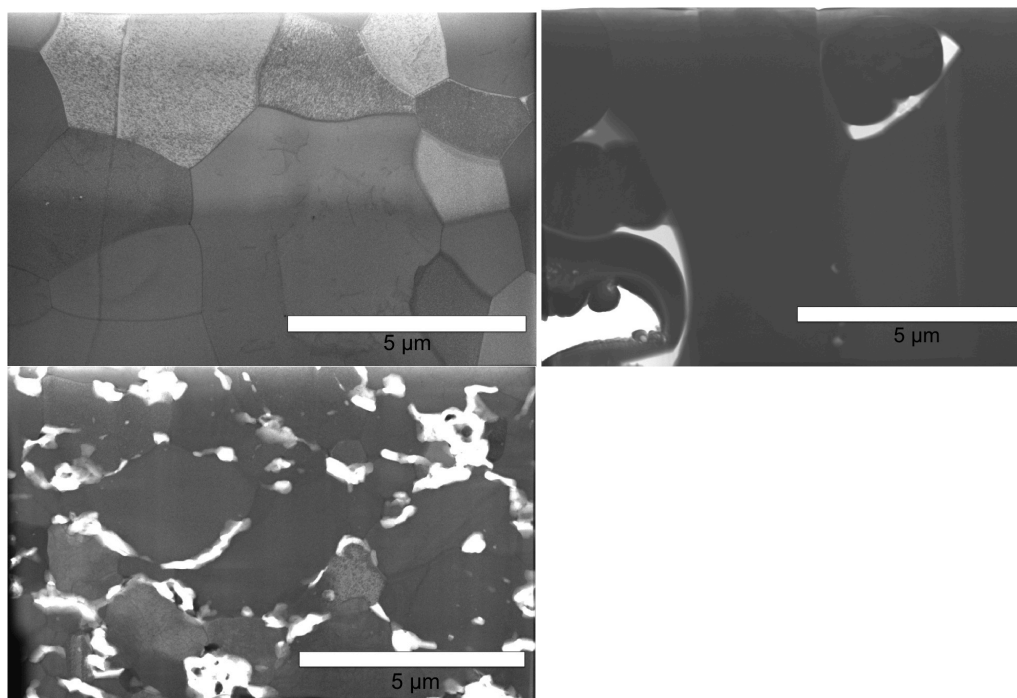


Figure 12. STEM images of AM0C (A), AM1C (B), and AM3C (C) all of which show evidence of carbon at the grain boundaries.

Electrical conductivity was measured as a function of temperature for all of the specimens to separate the electron and phonon contributions to thermal conductivity. Figure 13 shows that electrical conductivity for AM0C decreased with increasing temperature to a maximum value of $2.96 \times 10^4 \Omega^{-1}\text{cm}^{-1}$ at 300°C . The electrical conductivity decreased with 1 wt% carbon addition to $2.54 \times 10^4 \Omega^{-1}\text{cm}^{-1}$ and increased to $3.5 \times 10^4 \Omega^{-1}\text{cm}^{-1}$ with 3 wt% carbon addition at 300°C . For comparison, the magnitude of conductivity for the ZrB_2 ceramics in this study were comparable to that of nickel based alloys, which have a reported conductivity of $3.6 \times 10^4 \Omega^{-1}\text{cm}^{-1}$ at 300°C . Based on measured electrical conductivity, it appears that dissolution of carbon into the ZrB_2 matrix decreased its electrical conductivity and, therefore, the electron contribution to thermal conductivity in AM1C. In AM3C, the excess carbon formed ZrC and pulled W out of solid solution with ZrB_2 , forming $(\text{Zr,W})\text{C}$ which increased the electrical conductivity of AM3C compared to AM0C.

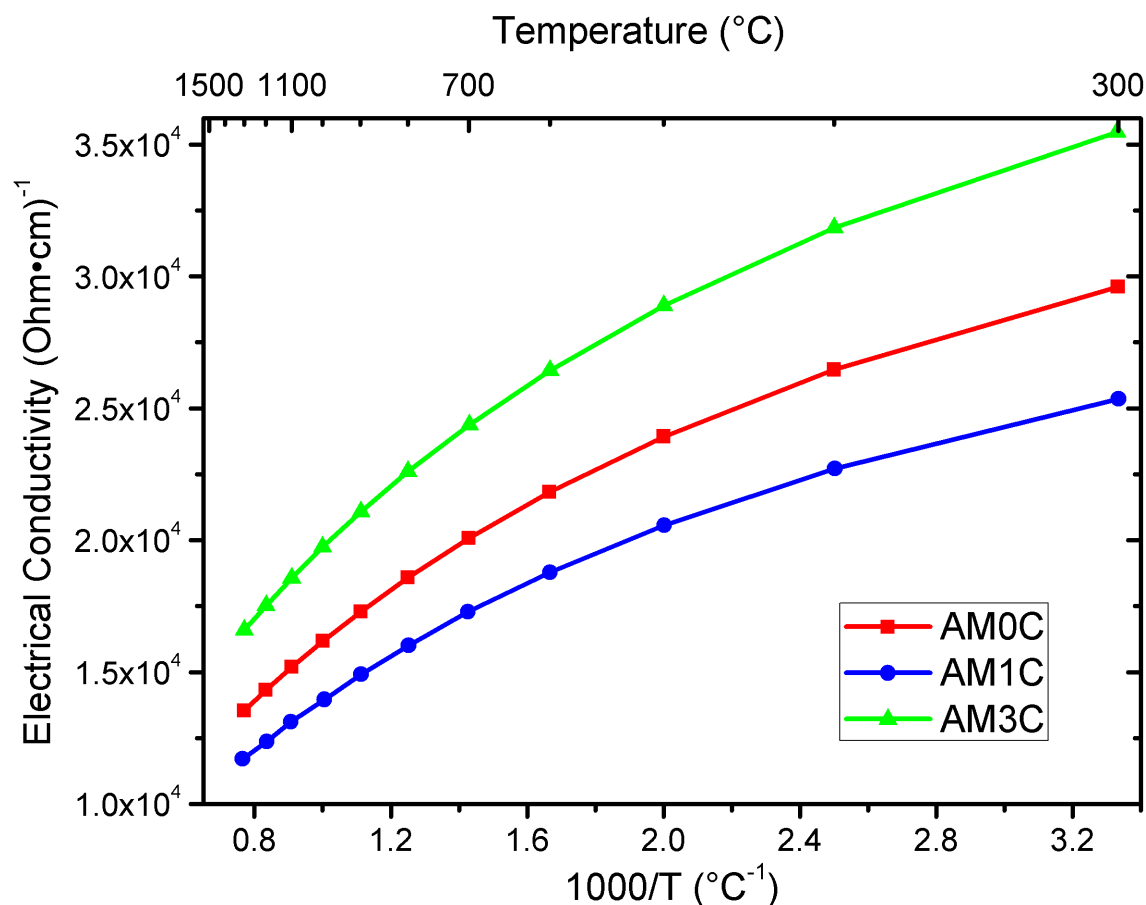


Figure 13. Electrical conductivity of AM0C, AM1C, and AM3C as a function of temperature.

The electron contribution to thermal conductivity was calculated from the electrical conductivity using the Wiedemann-Franz law. The phonon contribution was then estimated by subtracting the electron contribution from the total thermal conductivity. Figure 14 illustrates electron and phonon contributions to thermal conductivity as a function of temperature and carbon addition. Figure 14a shows that the electron contribution dominated thermal conductivity for AM0C, comprising about 90% of the total thermal conductivity at 2000°C. Figure 14b and c show the electron and phonon contributions to thermal conductivity for AM0C, AM1C and AM3C. The electron contribution displayed a similar trend with carbon addition as the overall thermal conductivity, wherein the addition of 1 wt% carbon led to a decrease in the electron contribution for all temperatures tested, but the addition of 3 wt% carbon led to an increase in the electron contribution. The presence of dissolved carbon in the ZrB₂ matrix in AM1C decreased the electronic portion of the conductivity due to solid solution formation, which decreased electrical conductivity of the ZrB₂ matrix. Interestingly, the addition of 1 wt% carbon did not appear to affect the overall phonon contribution to thermal conductivity as both AM0C and AM1C had phonon contributions of ~6 W/m•K at temperatures above 800°C. Thus, the dissolution of carbon into the ZrB₂ matrix did not appear to influence phonon transport, but decreased overall thermal conductivity of AM1C by decreasing the electron contribution to thermal conductivity.

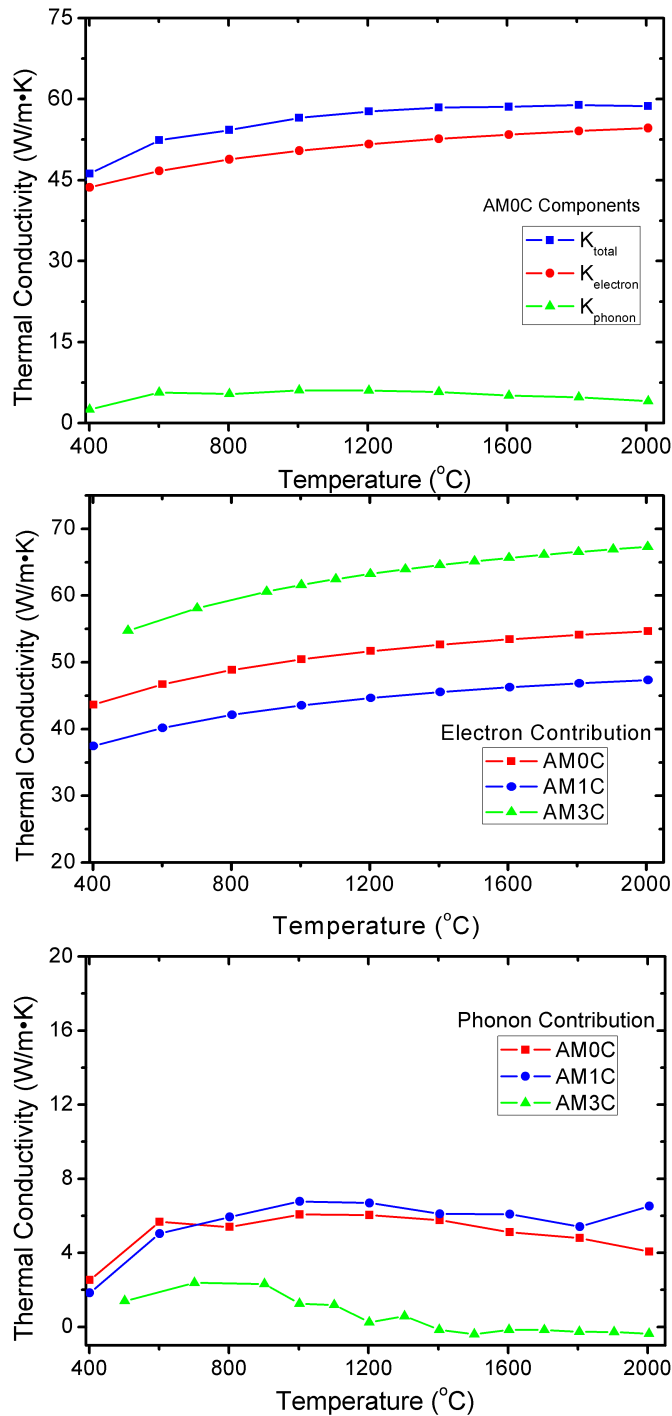


Figure 14. Electron and phonon contribution to thermal conductivity of AM0C, AM1C, and AM3C measured to 1200°C and extrapolated to 2000°C. AM0C total thermal conductivity with electron and phonon contributions is shown in (a), electron contributions of compositions in (b), and phonon contributions of compositions in (c).

In contrast to the lower carbon additions, AM3C had the highest value for the electron contribution to thermal conductivity with a value of 67 W/m•K at 2000°C compared to 47 W/m•K for AM1C and 54 W/m•K for AM0C. The increase in electron contribution, the dominant conduction mechanism for all of the specimens, was due to an increase in electrical conductivity. The increase was at least partially due to an increase in conductivity of the ZrB₂ matrix due to the reduced amount of W in solid solution in ZrB₂ after the formation of (Zr,W)C (2.67 vol%). The phonon contribution to thermal conductivity at 200°C decreased to near zero when 3 wt% carbon was added, compared to ~ 6 W/m•K for the AM0C and AM1C (Figure 14c). The decrease in the phonon contribution to thermal conductivity may have been due to the formation of graphite precipitates, which formed a percolating network of elongated and highly oriented graphite particles. Apparently, the formation of the second phase decreased phonon conduction. The overall increase in thermal conductivity of AM3C was, therefore, due to the increase in the electrical contribution that overcame a decrease in the phonon contribution. The increase in the electron contribution was due to the preferential migration of W from the ZrB₂ matrix to the newly formed ZrC phase when AM3C was heated to 2000°C.

The effect of W contamination that was noted above motivated a broader study of the effect of transition metals on the thermal conductivity of ZrB₂. For this part of the study, processing methods were modified to minimize the unintentional introduction of W as an impurity during powder processing. Zirconium diboride and phenolic resin were batched with either a transition metal boride or with elemental transition metal and boron powders to produce the compositions shown in Table 8. The starting powders were: ZrB₂ (Grade B, H.C. Starck), HfB₂ (Grade A, H.C. Starck), niobium (-325 mesh, 99.8%, Johnson Matthey), tungsten (<0.5µm, 99.9%, Johnson Matthey), TiB₂ (Grade HCT-F, Momentive), yttrium (-40 mesh, 99.9%, Alfa Aesar), and amorphous boron (SB Boron Corporation). Phenolic resin (Georgia Pacific) was added as a carbon source, which acted as a densification aid. With the exception of the composition with YB₂, the ZrB₂, transition metal, and boron powders were mixed by ball milling in acetone at 60 rpm for 24 hrs. Next, phenolic resin was added followed by ball milling at 30 rpm for one hour. Hexane was used as the solvent for the composition with YB₂ in an attempt to minimize contact between the yttrium powder and oxygen. The powders were dried by rotary evaporation at a temperature of 70 °C, vacuum of 68 kPa, and a rotation speed of 60 rpm. Powders were densified by hot pressing at 2150°C under 32 MPa pressure.

Table 8. Designation and composition after milling for tested ceramics.

Designation	Weight %			Atomic %					
	ZrB ₂	Carbon	TMB	Zr	TM	B	C	TM in Metal Sublattice	Metal to Boron Ratio
ZrB ₂	99.5	0.5	0.0	32.8	0.0	65.7	1.5	0.0	50.0
(Zr,Hf)B ₂	94.3	0.5	5.2	31.8	1.0	65.6	1.5	3.1	50.0
(Zr,Nb)B ₂	96.3	0.5	3.2	31.8	1.0	65.7	1.5	3.3	50.0
(Zr,W)B ₂	94.0	0.5	5.5	31.7	1.0	65.8	1.5	3.1	49.7
(Zr,Ti)B ₂	97.1	0.6	2.3	31.5	1.2	65.5	1.7	3.9	50.0
(Zr,Y)B ₂	96.7	0.4	2.9	31.9	1.0	65.7	1.4	3.0	50.0

With the exception of the composition with YB₂, the ZrB₂, transition metal, and boron powders were mixed by ball milling in acetone at 60 rpm for 24 hrs. Next, phenolic resin was added followed by ball milling at 30 rpm for one hour. Hexane was used as the solvent for the composition with YB₂ in an attempt to minimize contact between the yttrium powder and oxygen. The powders were dried by rotary evaporation at a temperature of 70 °C, vacuum of 68 kPa, and a rotation speed of 60 rpm. Powders were densified by hot pressing at 2150°C with an applied load of 32 MPa. The resulting billets were ground to produce parallel faces and cut into specimens that were either 12.7 mm by 12.7 mm by 2.5 mm rectangular prisms or 25.4 mm diameter by 1 mm tall cylinders. Archimedes method (ASTM standard C830-00) was used to determine the bulk density and apparent porosity of the specimens using vacuum infiltration with distilled water as the immersing medium. The bulk and crystallographic densities were then used to determine the relative density. Crystallographic densities were estimated from nominal compositions and lattice parameters determined using x-ray diffraction (XRD) analysis. For microstructure analysis, specimens were polished with diamond abrasive slurry to 0.25 μm and etched with potassium hydroxide at 210°C. The microstructure was investigated by imaging with scanning electron microscopy (SEM; S570 or S4700, Hitachi, Japan) and the grain size was determined by examining at least 150 grains per composition with image analysis software (ImageJ, National Institutes of Health, Bethesda, MD). The rectangular prisms were coated with graphite spray and used for measuring the thermal diffusivity, using the laser flash technique (Flashline 5000, Anter Corp, Pittsburg, PA) following ASTM standard E1461-11. The Clark and Taylor method was used to calculate the thermal diffusivity from the measured temperature rise times according to equations 8-10, where α is the thermal diffusivity (cm²/s), K_R is the Clark and Taylor correction factor, L is the thickness of the specimen (cm), and t_n is the time required for the temperature to increase by the designated fraction (s).

$$\alpha_{corrected} = \frac{\alpha K_R}{0.13885} \quad (8)$$

$$\alpha = 0.1388 \frac{L^2}{t_{0.50}} \quad (9)$$

$$K_R = -0.3461467 + 0.361578 \left(\frac{t_{0.75}}{t_{0.25}} \right) - 0.06520543 \left(\frac{t_{0.75}}{t_{0.25}} \right)^2 \quad (10)$$

An exponential fit was applied to the thermal diffusivity data and the values were corrected for porosity assuming the relationship shown in Equation 11, where α is the diffusivity (cm²/s) and P is the volume fraction of porosity.

$$\alpha = \alpha_{fit} / (1 - P) \quad (11)$$

The resulting trend line for thermal diffusivity was combined with the temperature-dependent density, and the heat capacity values from NIST-JANAF to calculate the thermal conductivity using Equation 12, where k is the thermal conductivity (W/m•K), α is the thermal diffusivity (cm²/s), ρ is the density (g/cm³), C_p is the heat capacity (J/mol•K), and M is the molar mass (g/mol). The temperature-dependent density values were determined from measured Archimedes bulk density and the linear expansion data for polycrystalline ZrB₂ from Touloukian.

$$k = \frac{\left(\frac{100cm}{m} \right) \alpha \rho C_p}{M} \quad (12)$$

Table 9 summarizes the microstructural characteristics of the materials examined in this study including measured bulk density, porosity, and average grain size. In addition, the crystallographic density was calculated from the nominal compositions. All of the ceramics reached >98.5% relative density. Archimedes measurements indicated that the specimens had negligible open porosity.

Table 9. Designation, density, porosity, and average grain size for tested compositions

Designation	Theoretical Density	Bulk Density	Relative Density	Porosity	Grain Size
	g/cm ³	g/cm ³	%	%	μm
ZrB ₂	6.05	5.97	98.6	1.4	22 +/- 20
(Zr,Hf)B ₂	6.20	6.17	99.5	0.5	29 +/- 27
(Zr,Nb)B ₂	6.08	6.04	99.3	0.7	8 +/- 10
(Zr,W)B ₂	6.23	6.29	99.9 +	0.0	19 +/- 17
(Zr,Ti)B ₂	6.00	5.95	99.2	0.8	27 +/- 25
(Zr,Y)B ₂	6.02	6.01	99.8	0.2	19 +/- 16

The transition metal additions dissolved into the ZrB₂ to produce single phase ceramics. Figure 15 shows the measured thermal diffusivity values for all of the compositions. The diffusivity data were fit with an exponential trend line, $\alpha = ae^{b/T}$, where T is temperature in Kelvin. The trend line was then corrected for porosity using the relationship shown in equation 11. The values for a and b , as well as the regression of the fits, are shown in Table 15.

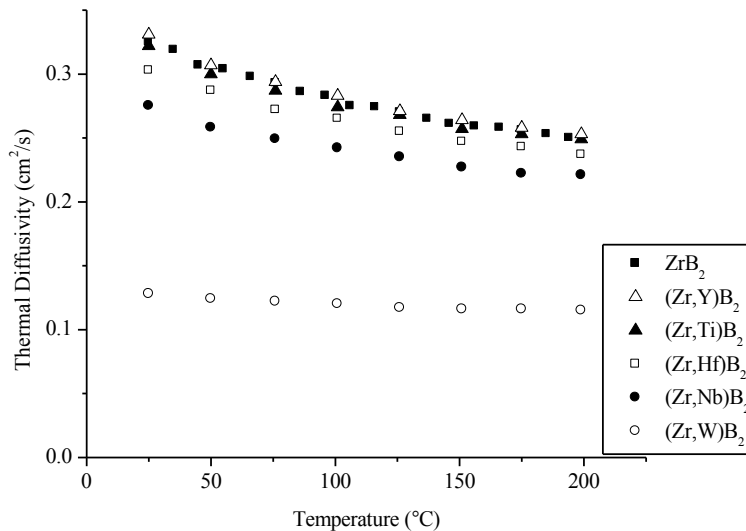


Figure 15. Measured thermal diffusivity as a function of temperature for ZrB₂ with transition metal additions.

Table 10. Fitting parameters for thermal diffusivity data for all of the compositions

	Composition					
	ZrB ₂	(Zr,Hf)B ₂	(Zr,Nb)B ₂	(Zr,W)B ₂	(Zr,Ti)B ₂	(Zr,Y)B ₂
a (cm ² /s)	0.1572	0.1561	0.1502	0.0943	0.1588	0.1602
b (K)	215.85	196.41	177.91	89.89	207.40	212.66
Regression	0.9967	0.9975	0.9918	0.9897	0.9940	0.9950

Figure 16 shows calculated thermal conductivities for all of the compositions. Nominally pure ZrB₂ had the highest thermal conductivity with a value of 87 W/m•K at 25°C that decreased to 85 W/m•K at 200°C. The room temperature thermal conductivity of nominally pure ZrB₂ produced in the present study is consistent with values reported for fully dense phase-pure ZrB₂ produced from commercial powder. The addition of yttrium or titanium to ZrB₂ had almost no effect on the thermal conductivity of the resulting solid solutions. At room temperature the thermal conductivity was 87 W/m•K for (Zr,Y)B₂ and (Zr,Ti)B₂. The thermal conductivities decreased slightly as temperature increased to 200°C, with values of 86 W/m•K for both (Zr,Y)B₂ and (Zr,Ti)B₂. Apparently, some transition metal additions do not impact the thermal properties of ZrB₂. Both Y and Ti have lower atomic numbers and masses than Zr and are positioned directly to the left (Y) and above (Ti) Zr in the periodic table. The addition of hafnium and niobium diboride decreased the thermal conductivities of the resulting ceramics. At 25°C, the thermal conductivities were 81 W/m•K for (Zr,Hf)B₂ and 74 W/m•K for (Zr,Nb)B₂. At 200°C, the values were 81 W/m•K and 75 W/m•K, respectively. Decreases between 4% and 16% compared to the nominally pure composition. In this case, both Hf, and Nb have higher atomic numbers and are heavier than Zr with Hf lying below and Nb to the right of Zr in the periodic table. The most significant impact on thermal conductivity was observed when W was added. The room temperature thermal conductivity of (Zr,W)B₂ was 34 W/m•K, which increased slightly to 39 W/m•K at 200°C. Both are a decrease of more than 50% compared to nominally pure ZrB₂. Interestingly, (Zr,W)B₂ was the only composition to exhibit a noticeable increase in thermal conductivity with increasing temperature for the range of temperatures tested. Combined with the observations from the other additions, it appears that the effect of transition metals on thermal conductivity increases moving down and right across the periodic table. Moving across a row to the right appears to have a stronger effect than moving down in a column.

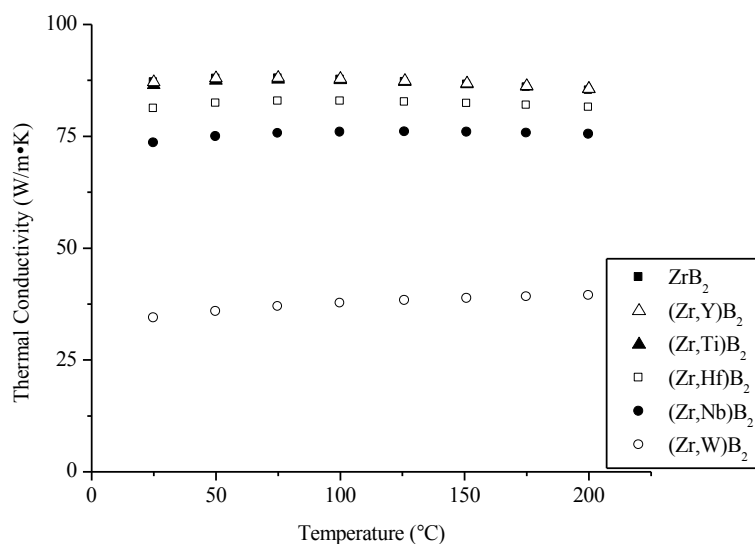


Figure 16. Thermal conductivity as a function of temperature for ZrB₂ with various transition metal additions.

Figure 17 shows the electrical resistivity values that were measured for all of the compositions. The electrical resistivity values follow a trend similar to the inverse of the thermal conductivity. Whereas the room temperature thermal conductivity of ZrB₂ was the highest, the room temperature resistivity measurement of ZrB₂ was the lowest, 8.9 $\mu\Omega\text{-cm}$. The hafnium, titanium, and yttrium additions also had the smallest impact, only raising the resistivity slightly to 9.2, 9.2, and 9.8 $\mu\Omega\text{-cm}$ respectively, (<10% increase). The niobium and tungsten additions had a larger influence, raising the resistivity to 11.6, and 30.3 $\mu\Omega\text{-cm}$ respectively, (30 and 240% increases).

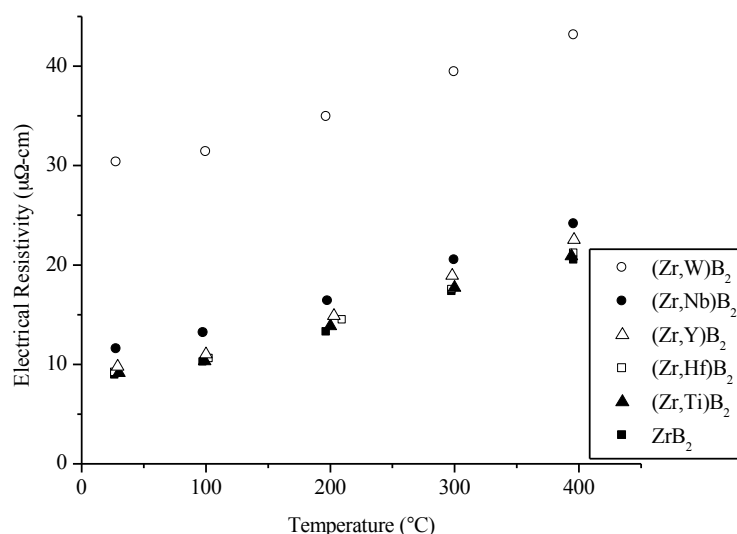


Figure 17. Electrical resistivity as a function of temperature for ZrB₂ with various transition metal additions.

The electrical resistivity data were fit to a linear trend line, $\rho = aT + b$, where T is temperature in Kelvin. The values for a and b as well as the regression of the fits are listed in Table 11. The resistivity fit was inverted to find the electrical conductivity, which was then used to calculate the electron contribution to the thermal conductivity using the theoretical Lorenz number, and the Wiedemann-Franz law

Table 11. Fitting parameters for electrical resistivity of all of the compositions.

	Composition					
	ZrB ₂	(Zr,Hf)B ₂	(Zr,Nb)B ₂	(Zr,W)B ₂	(Zr,Ti)B ₂	(Zr,Y)B ₂
a	0.0323	0.0332	0.0348	0.0363	0.0334	0.0360
b	-1.3836	-1.3696	0.5539	18.5220	-1.5723	-1.7768
Regression	0.99	0.9919	0.9926	0.9847	0.9915	0.9896

Figure 18 summarizes the electron contribution to thermal conductivity calculated from measured electrical resistivity using the Wiedemann-Franz law. The phonon contribution to thermal conductivity was estimated by subtracting the value for the electron contribution from the total thermal conductivity. For all of the specimens, the electron contribution was much larger than the phonon contribution. Additives lowered the electron contribution to thermal conductivity of ZrB₂ in a trend that was similar to total thermal conductivity. The main difference was that any addition reduced the electron contribution to thermal conductivity, not just moving down or to the right on the periodic table. For example, the addition of group IVb metals such as Ti and Hf (i.e., the same as zirconium) resulted in small (<5%), but repeatable decreases in the electron portion of thermal conductivity. For ZrB₂, the electron contribution was 88 W/m•K compared to 85 W/m•K for (Zr,Hf)B₂ and 87 W/m•K for (Zr,Ti)B₂. The

addition of metals from different groups resulted in larger decreases in the electron contribution to thermal conductivity. The electron contributions to thermal conductivity were 81 W/m•K for (Zr,Y)B₂ (8% decrease, group IIIb), 67 W/m•K for (Zr,Nb)B₂ (24% decrease, group Vb), and 25 W/m•K for (Zr,W)B₂ (72% decrease, group VIb). The phonon contribution to thermal conductivity was calculated by subtracting the electron contribution from the total thermal conductivity. The differences between the changes in total thermal conductivity and those of the electron and phonon portions indicate that certain additives have a larger impact on electron conduction, while others have a greater influence on phonon conduction. For example, (Zr,Ti)B₂ and (Zr,Y)B₂ decreased the electron contribution, but increased the phonon contribution by roughly equal amounts (7 and 1 W/m•K respectively). Although neither additive changed the total thermal conductivity at room temperature, the addition of Y had a greater influence on the electron and phonon contributions to thermal conductivity than Ti. (Zr,W)B₂ decreased the electron contribution by ~60 W/m•K but increased the phonon contribution by ~10 W/m•K. Even though the addition of W increased the phonon contribution, similar to Y, it resulted in a significant decrease in the electron contribution, resulting in a net decrease in thermal conductivity. The reason for the apparent increase in phonon conductivity with the addition of W is not clear, but it could be due to the use of the theoretical Lorenz number in the calculation of the electron contribution. It seems reasonable that the addition of W decreased both the electron and phonon contributions by changing the mean free paths for phonon and electron conduction, but measuring those quantities to determine the actual Lorenz number for (Zr,W)B₂ was beyond the scope of the present study. In some cases, a negative phonon contribution to thermal conductivity was calculated. Obviously, negative phonon contributions are not physically possible. As with the addition of W discussed above, the Lorenz number for ZrB₂ and ZrB₂ with transition metal additives should have a smaller value than L_0 .

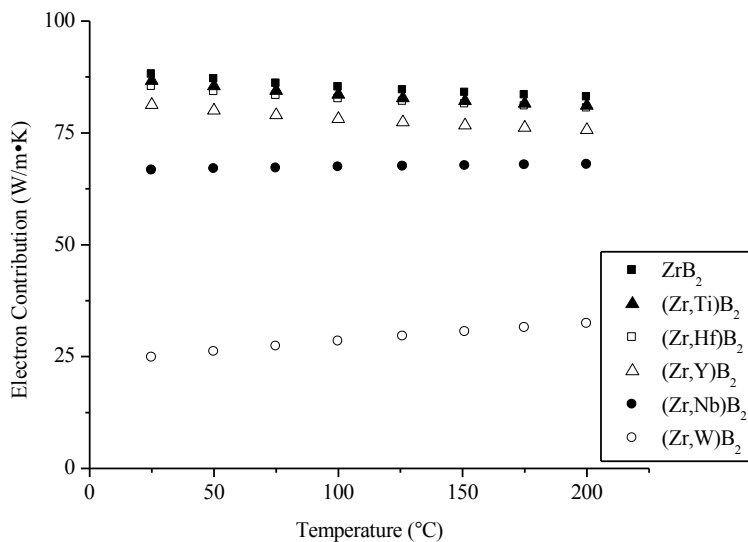


Figure 18. Electron contribution to thermal conductivity.

XRD analysis was used to determine the lattice parameters for each composition produced in the present study. The measured lattice parameters are summarized in Table 12. In addition, the unit cell volume and percent change in unit cell volume compared to nominally pure ZrB₂ were also calculated. Figure 19 shows the calculated volume change vs. the total

thermal conductivity. For the addition of Y, Hf, and Nb, the total thermal conductivity decreased in direct proportion to the volume change induced by substitution of the other metal into the ZrB_2 lattice. These additives change the lattice parameters of the ZrB_2 when they go into solid solution. The addition of Ti did not follow this trend, as the thermal conductivity of $(\text{Zr,Ti})\text{B}_2$ was higher than expected based on the change in lattice parameter. Unlike the pure diborides of the other additives, the lattice parameters of TiB_2 are controlled by the B-B bond lengths, not the bonds in the close packed Ti layer (a-lattice parameter) or the Ti-B bonds (c-lattice parameter) due to the smaller size of the titanium atom compared to zirconium. The total thermal conductivity of $(\text{Zr,W})\text{B}_2$ was lower than expected based on the measured change in the unit cell volume. The addition of W may have decreased the thermal conductivity more than expected due to the structure of W-borides. Unlike the diborides of the other additives examined in this study, the W-borides have a different structure, $\text{P6}_3/\text{mmc}$ for W_2B_5 compared to $\text{P6}/\text{mmm}$ for the other diborides examined in the present study. Thus, in addition to the change in lattice parameters and volume, the addition of W may be inducing additional strain into the ZrB_2 lattice due to the different structure of W-borides. Regardless, using the lattice parameters, especially combined with atom location on the periodic table, may be a suitable way for predicting the thermal properties of ZrB_2 -based ceramics.

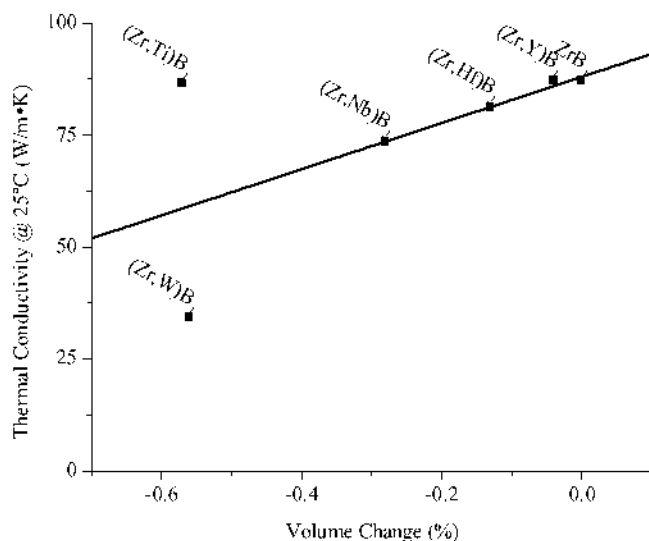


Figure 19. Relationship between volume change and the total thermal conductivity

Table 12. Summary of lattice parameters and unit cell volumes.

Composition	Measured Lattice Parameters			
	a (Å)	c (Å)	Volume (Å ³)	Volume Change (%)
ZrB ₂	3.16814(2)	3.52992(5)	30.683	0
(Zr,Hf)B ₂	3.16689(2)	3.52828(5)	30.645	-0.13
(Zr,Nb)B ₂	3.16565(5)	3.52552(11)	30.597	-0.28
(Zr,W)B ₂	3.16296(2)	3.52161(5)	30.511	-0.56
(Zr,Ti)B ₂	3.16283(2)	3.52163(7)	30.509	-0.57
(Zr,Y)B ₂	3.16754(2)	3.52986(5)	30.671	-0.04

Ultra-High Temperature Mechanical Properties

An ultra-high temperature atmosphere-controlled mechanical testing was completed as part of the present project. The system, shown in Figure 20, is capable of testing at temperatures up to 2600°C. The ultra-high temperature test system, which consists of a screw driven universal test frame equipped with a custom-built environmental chamber and an inductively heated hot zone with a graphite susceptor. The environmental chamber is capable of operating in inert or reducing atmospheres, or mild vacuum (to about 35 kPa). The furnace temperature is regulated using a PID (proportional integral derivative) controller with temperatures measured by a type-B thermocouple below 1600°C and a two-color pyrometer above 1500°C. Heating rates as high as 500°C/min have been achieved. To date, four point bend tests as described by ASTM C1211 (Flexural Strength for Advanced Ceramics at Elevated Temperature) have been performed, but the system is capable of conducting tensile and compression tests with the proper test fixtures.

The system originally was designed for testing at temperatures up to 2500°C. One approach would be to purchase a traditional graphite or refractory element vacuum furnace and integrate it into an existing test frame. However, these types of furnaces raised several concerns including chemical compatibility with fixturing and specimens at elevated temperatures; limited heating rates; and atmosphere limitations. Selecting an induction furnace overcame some of these limitations. One advantage of induction heating is the ability to change the hot zone material and test fixturing based on the type of material being tested and the atmosphere required. Induction furnaces also enable higher heating and cooling rates than graphite element resistance furnaces, which allows for testing multiple specimens per day. The drawback to this approach was that no commercially available systems appeared to meet the intended design requirements.

The most significant challenges encountered during construction of the system were related to the induction coil. During initial testing, the original induction coil did not have sufficient electrical insulation to operate in an environment with graphite dust, which caused the coil to electrically short to the insulation pack surrounding the susceptor. The short melted a portion of the coil and burned a hole through the insulation. Adding several additional layers of electrical and thermal tape isolated the coil from the graphite insulation pack. For the current design, the coil was wrapped with mica tape, followed by fiberglass tape, and finally covered with Nextel sleeving. A sheet of alumina paper further isolated the graphite insulation from the induction coil. This furnace design has been tested successfully up to 2600°C.

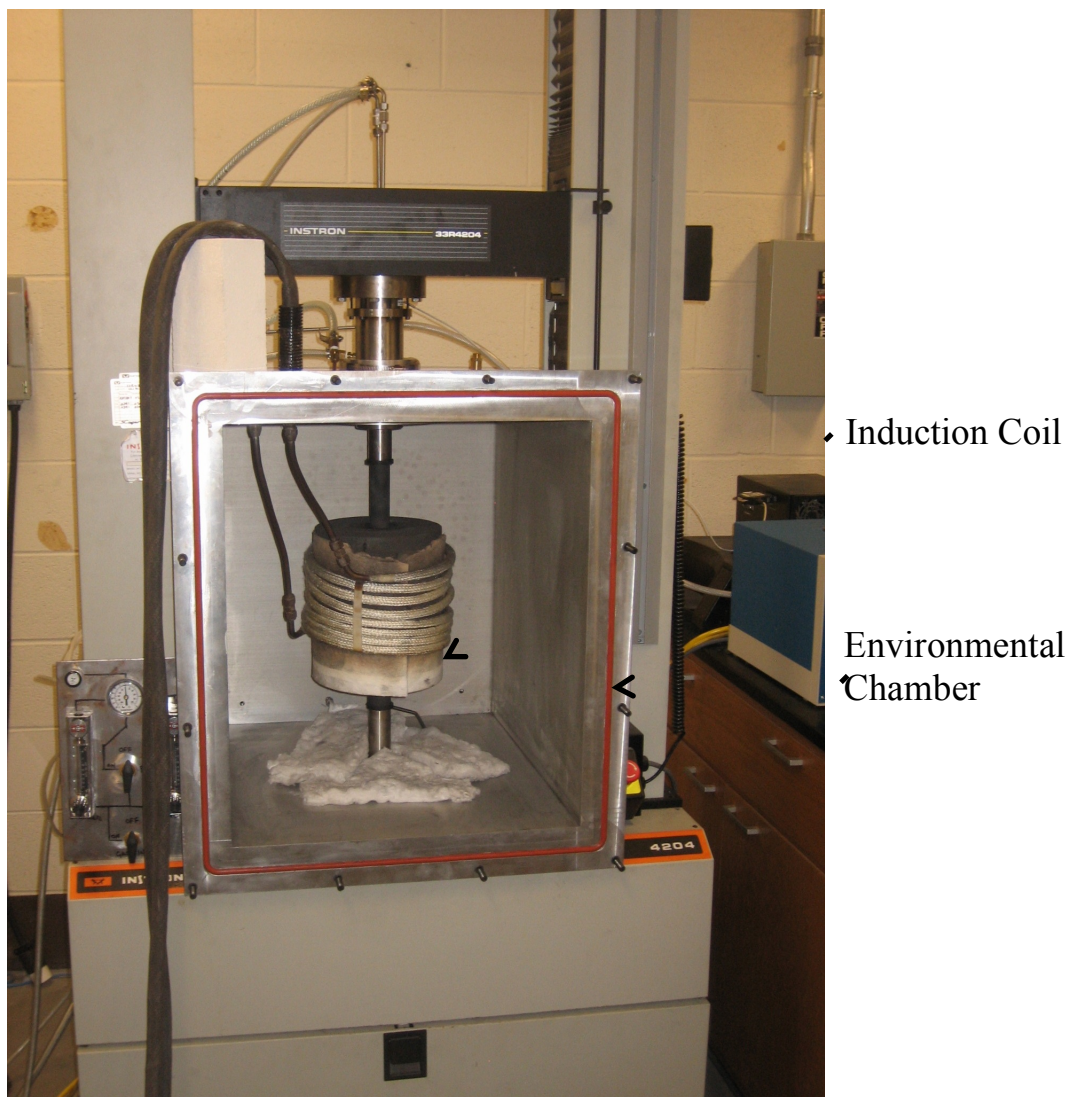


Figure 20. Ultrahigh temperature mechanical testing apparatus showing the environmental chamber, induction coil, and test frame.

The first study conducted with the ultra-high temperature testing system was to examine the strength of ZrB_2 at temperatures as high as possible. With the original graphite test fixture, the testing temperature is limited to about 2300°C due to the $\text{ZrB}_2\text{-C}$ eutectic, which occurs at about 2390°C . Dense ZrB_2 was prepared by hot pressing at 2150°C . Graphite was added in the amount of 0.5 wt% as a densification aid. Although ZrB_2 with graphite additions can be densified at lower temperatures, 2150°C was selected for the present study to produce a relatively large grain size and minimize the effects of creep during elevated temperature testing.

Room and elevated temperature flexure strengths were measured following ASTM C1161 and ASTM C1211, respectively, in four-point bending using a fully-articulated test fixture and type-B bars (45 mm x 4 mm x 3 mm). Five specimens were tested at room temperature and three at each elevated temperature (Table 13). Bars were machined from the hot-pressed billets by diamond grinding on a fully automated surface grinder. Tensile surfaces were polished to $1\ \mu\text{m}$ using diamond abrasives. Specimens tested in air were coated with silica

by dipping in a sol prepared from tetraethylorthosilicate, then heat treating to 800°C in air. Tests in air were performed using a screw-driven instrumented load frame (5881, Instron, Norwood, MA) and a molybdenum disilicide element furnace (MDS66C, Instron SFL, Thornbury, Bristol). A deflectionometer was used to record bar displacement. The heating rate for all elevated temperature tests was 10°C/min followed by an isothermal hold for 10 min at the desired temperature. Room temperature elastic constants were determined by impulse excitation (MK4-I Grindosonic, J.W. Lemmens, St. Louis, MO) according to ASTM C1259. The static bend test method was used to determine the elevated temperature elastic modulus of specimens tested in air according to ASTM standard E111. A minimum of three measurements were averaged to calculate the reported values.

As described above, a mechanical testing apparatus consisting of a screw-driven instrumented load frame (33R4204, Instron, Norwood, MA), induction heated graphite hot zone inside an environmental chamber was built to perform testing up to 2600°C. Temperature was controlled using a two-color optical pyrometer and a programmable PID controller. Water cooled graphite pushrods and a fully articulated graphite 4-point bend fixture based on Grathwohl's design were used. Specimens were loaded onto the fixture and secured using a cyanoacrylate adhesive. The environmental chamber was evacuated to ~35kPa and backfilled with argon five times and then argon purged for an additional 30 minutes prior to heating. Specimens were heated at ~100°C/min to 200°C below the test temperature, then heated at 50°C/min to the test temperature followed by a 5 min isothermal hold. Tests were conducted at a crosshead rate of 10 mm/min to 10N, followed by the minimum crosshead rate that resulted in linear elastic behavior (Table 13) until failure.

Table 13. Elevated temperature mechanical properties measured ZrB₂ ceramics.

Temperature (°C)	Atmosphere	Crosshead rate (mm/min)	Elastic modulus (GPa)	Strength (MPa)
RT	Air	0.5	524 ± 17	381 ± 41
1000	Air	0.5	414 ± 34	399 ± 37
1200	Air	0.5	392 ± 36	392 ± 37
1300	Air	0.5	368 ± 16	236 ± 3
1400	Air	1.0	297 ± 6	176 ± 18
1500	Argon	1.5	--	173 ± 6
1600	Air	2.0	263 ± 23	110 ± 11
1600	Argon	2.0	--	212 ± 26
1800	Argon	2.5	--	220 ± 18
2000	Argon	3.0	--	223 ± 18
2200	Argon	3.5	--	299 ± 5
2300	Argon	5.0	--	216 ± 40

The resulting relative density of the test specimens was 99.4%. Figure 21 shows a typical cross section of polished and chemically etched ZrB₂. The grain size was 19.4 ± 13.0 µm. Approximately 0.4% porosity was observed within grains, on the grain boundaries, and at triple grain junctions. The size of the closed pores was in the range of 0.5 to 2.5 µm. No residual C was observed. The amount of carbon added as a sintering aid (~0.5 wt%) was less than the reported

solubility limit (~ 1.2 wt%) at the processing temperature (2150°C). Likewise, no WC was observed as its content was below its reported solubility limit of ~ 8 mol%. Thus, both C and WC dissolved into the ZrB_2 matrix

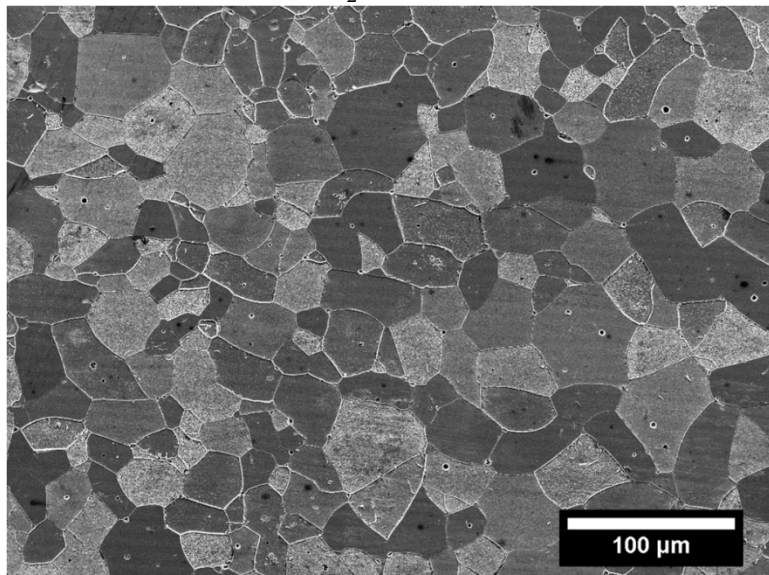


Figure 21. SEM image of a polished and chemically etched cross-section of ZrB_2 ceramic.

Elastic modulus was measured for specimens tested in air. The room temperature modulus was 524 GPa, which was higher than values of 490 GPa to 500 GPa that are typically reported for nominally pure ZrB_2 . However, the values are similar to those reported for ZrB_2 with B_4C and C additives, which lie in the range of 510 GPa to 530 GPa. As temperature increased, the modulus decreased in an apparent linear trend from ~ 524 GPa at room temperature to ~ 370 GPa at 1300°C (Figure 22). The modulus decreased more rapidly above 1300°C to ~ 260 GPa at 1600°C . These elastic moduli values were similar to values reported by Rhodes^{*} and Zhu.[†] As also reported by Zhu, the values exhibited a transition around 1300°C . This change in behavior was previously attributed to softening of grain boundaries or second phases isolated at triple grain junctions by Rhodes.

Figure 23 shows the flexure strength as a function of temperature and testing atmosphere. Strengths were tested in air up to 1600°C and in argon from 1500°C to 2300°C (Table 13). Strengths did not change significantly up to 1200°C (~ 390 MPa), but dropped from ~ 390 MPa at 1200°C to ~ 110 MPa at 1600°C . However, testing in argon revealed that strength increased from ~ 170 MPa at 1500°C to ~ 210 MPa at 1600°C . Previous analysis by Watts et al. determined that residual thermal stresses in ZrB_2 ceramics relaxed at 1400°C , which could account for the drop in strength between 1200°C and 1400°C . The strength increased to ~ 220 MPa at 1800°C and 2000°C . A similar increase in strength was observed by Rhodes *et al.*, and was attributed to stress relief through plastic flow. Whereas Rhodes observed a strength maximum at 1800°C , the present study observed near constant strength between 1600°C and 2000°C . The drop in strength

^{*} W.H. Rhodes, E.V. Clougherty, and D. Kalish, "Research and Development of Refractory Oxidation-Resistant Diborides Part II, Volume IV: Mechanical Properties," Technical Report AFML-TR-68-190, Part II, Volume IV, ManLabs Incorporated and Avco Corporation, Wright Patterson Air Force Base, OH, 1970.

[†] S. Zhu, "Densification, Microstructure, and Mechanical Properties of Zirconium Diboride Based Ultra-High Temperature Ceramics"; Ph.D. Thesis. Missouri University of Science and Technology, Rolla, 2008

above 1800°C reported by Rhodes is likely due to creep above 1600°C that resulted from the use of a constant strain rate for all temperatures. In the present study, strain rate was increased with temperature to achieve linear elastic failure and avoid creep as called for in ASTM C1211. The strength increased to nearly 300 MPa at 2200°C, which was above the processing temperature of 2150°C. The increase in strength at 2200°C could be due to further sintering of the material or solutionization reactions, but requires further analysis. Testing was limited to 2300°C due to the ZrB₂-C eutectic at ~2390°C, which would result in melting due to interaction of the specimen with the test fixture at higher temperatures. Use of a ZrC test fixture could enable testing up to ~2600°C.

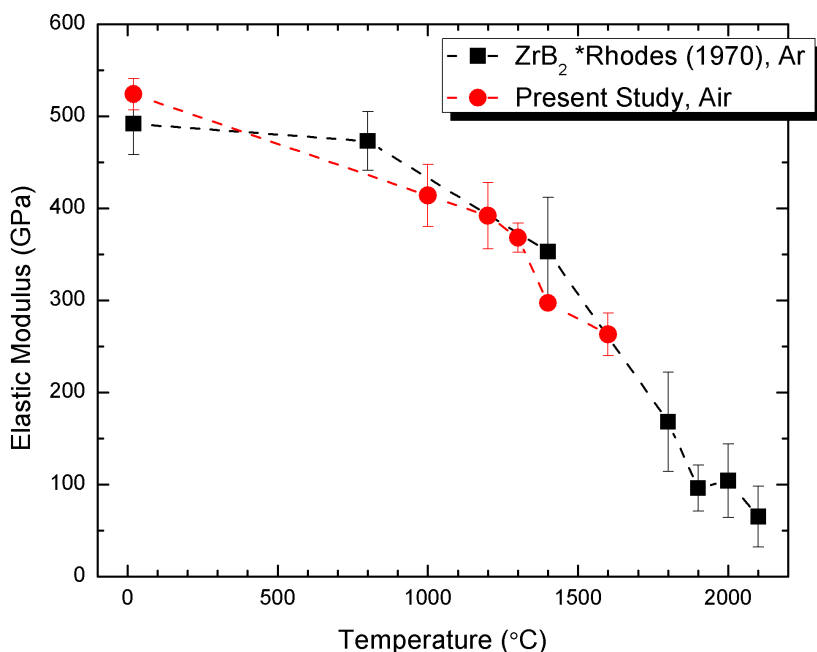


Figure 22. Elastic modulus of ZrB₂ tested in air atmosphere as a function of temperature

Strength at room temperature was ~380 MPa, which was higher than that reported by Rhodes (326 MPa) for ZrB₂ with similar grain size and density. Strengths in the range of 380 MPa to 570 MPa have been reported for ZrB₂ with smaller average grain sizes and/or second phases. The ceramic examined in the present work had an average grain size of nearly 20 μm, which reduced its room temperature strength compared to finer grained ZrB₂, but should reduce creep and improve strength at elevated temperatures compared to the finer grained ceramics. In addition, the strength of the ceramic used in the present study increased above 2000°C, maintaining a value of ~220 MPa, whereas Rhodes reported degradation of strength above 1900°C. The improved strength above 1900°C could be due to the higher purity of the modern powders compared to those used by Rhodes. The improved purity would reduce the presence of second phases (e.g., ZrO₂ in Rhodes material), which could reduce grain boundary softening and result in a stiffer material at elevated temperatures. Further, unlike the work reported by Rhodes, which noted significant creep, higher strain rates were used at elevated temperatures to achieve brittle failure without creep during testing. The ZrB₂ in this study exhibited a room strength

similar to that found previously in ZrB_2 with a finer microstructure, while elevated temperature strength benefited from a lower impurity content.

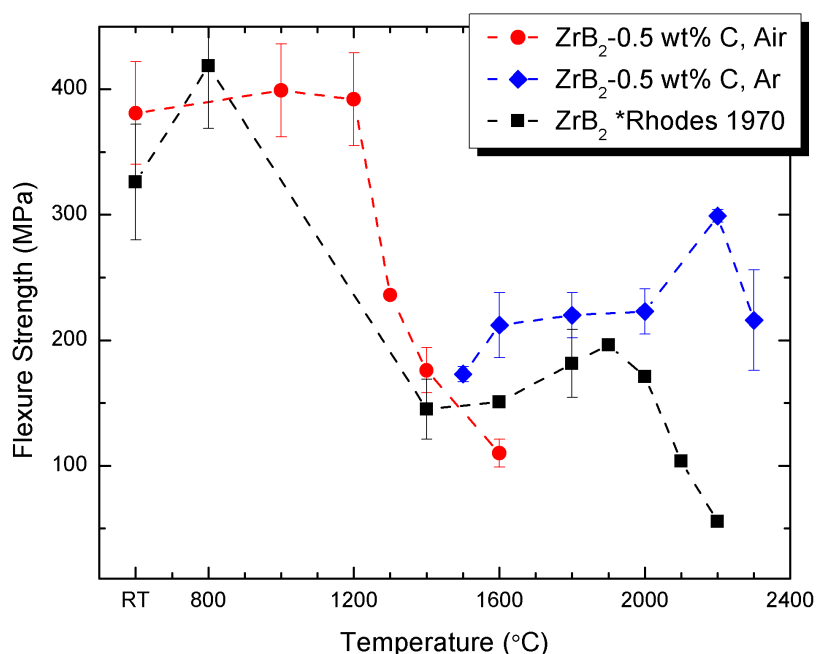


Figure 23. Four-point flexure strength of ZrB_2 ceramics tested in air (circles) and argon (diamonds) atmospheres as a function of temperature. For comparison, the data of Rhodes et al. (squares) are also shown.

The strength of ZrB_2 -SiC ceramics was also examined. Commercially available ZrB_2 powder (Grade B, H.C. Starck, Newton, MA) and SiC (Grade UF-10, H.C. Starck) were used to prepare the specimens. Boron carbide (Grade HD-20, H.C. Starck) was used as a sintering aid. The powders were batched in the ratio of 70 vol% ZrB_2 to 30 vol% SiC with a super addition of 2 wt% B_4C (ZrB_2 basis). The powders were mixed by ball milling with WC-6Co media in acetone with dispersant (DISPERBYK®-110, BYK-Gardner USA, Columbia, MD). After ball milling for 24 hours, the slurry was dried by rotary evaporation (Model Rotavapor R-124, Buchi, Flawil, Germany) at a temperature of 70°C, low vacuum (~27 kPa), and a rotation speed of 60 rpm. The powders were densified by hot pressing at 1950°C.

The bulk density of the hot pressed specimens was measured by Archimedes' method using distilled water as the immersing medium as described in ASTM C373-88. Microstructures were examined using scanning electron microscopy (SEM; S570, Hitachi, Tokyo, Japan). Specimens were prepared for microscopy by cutting cross sections perpendicular to the hot-pressing direction and polishing to a 0.25 μm finish using diamond abrasives. The ZrB_2 was etched using molten KOH at 450°C for 1 s. The SiC was etched using boiling Hall's Reagent for 20 min. ZrB_2 and SiC grain sizes were measured from SEM images using computerized image analysis (ImageJ, National Institutes of Health, Bethesda, MD). The grain size distribution was determined by measuring the equivalent area diameter of at least 1000 grains of both ZrB_2 and

SiC. The SiC and B₄C cluster size distribution was determined from the polished cross sections by measuring the Feret's diameter of at least 45,000 and 15,000 clusters.

Room temperature flexure strengths were measured in four-point bending using a fully-articulated test fixture using type-B bars (45 mm x 4 mm x 3 mm) according to ASTM C1161-02c. Flexure strength was measured at elevated temperatures (800, 1000, 1200, 1400, 1500, and 1600°C) using the same type-B bars and following the testing procedures outlined in ASTM C1211-08. Nine specimens were tested at room temperature and a minimum of five specimens were tested at each elevated temperature. Bars were machined from the hot-pressed billets by diamond grinding on a fully automated surface grinder (FSG-3A818, Chevalier, Santa Fe Springs, CA). The flexure surface was polished to 1 µm using diamond abrasives. Tests were performed using a screw-driven instrumented load frame (5881, Instron, Norwood, MA). Elevated temperature testing was performed in a molybdenum disilicide element furnace (MDS66C, Instron SFL, Thornbury, Bristol). A deflectionometer was used to record the displacement of the test bars during loading. A crosshead rate of 0.5 mm/min was used up to 1200°C, 1.5 mm/min at 1400°C, 2.0 mm/min at 1500°C, and 2.5 mm/min at 1600°C. The heating rate for all of the high temperature tests was 10°C/min followed by an isothermal hold for 10 min at the desired temperature before testing.

The measured bulk densities of the hot-pressed specimens were 5.22 g/cm³. The theoretical density calculated from the nominal composition (67.75 vol% ZrB₂, 29.00 vol% SiC, and 3.27 vol% B₄C) plus milling contamination (0.24 – 0.32 wt% WC-6Co) was determined to be 5.15 g/cm³. The composition after hot pressing was determined by image analysis to be 68.5 vol% ZrB₂, 29.5 vol% SiC, and 2.0 vol% B₄C, giving a theoretical density of 5.18 g/cm³. Porosity was not observed in the hot pressed specimens. Further, if the density of ZrB₂ is adjusted for the reported hafnium content in the starting powder (~1.9 wt%), the predicted theoretical density increases to 5.22 g/cm³. Therefore, the measured bulk density is consistent with SEM observations that the specimens were fully dense.

Figure 24 shows a typical cross section of a polished and a chemically etched specimen. The ZrB₂ and SiC grain sizes were measured as 1.9 ± 0.9 µm and 1.2 ± 0.5 µm respectively. Approximately 2.0 vol% B₄C, which was added as a sintering aid, was observed in the microstructure following hot pressing. The B₄C grain size was not measured, as a suitable etch could not be found to reveal the B₄C grain boundaries. The B₄C cluster size was measured to be 1.2 ± 1.0 µm with a maximum cluster size of 14.4 µm. The SiC particles were found to segregate into large clusters (6.1 ± 4.4 µm) with a maximum measured cluster size of 58.9 µm.

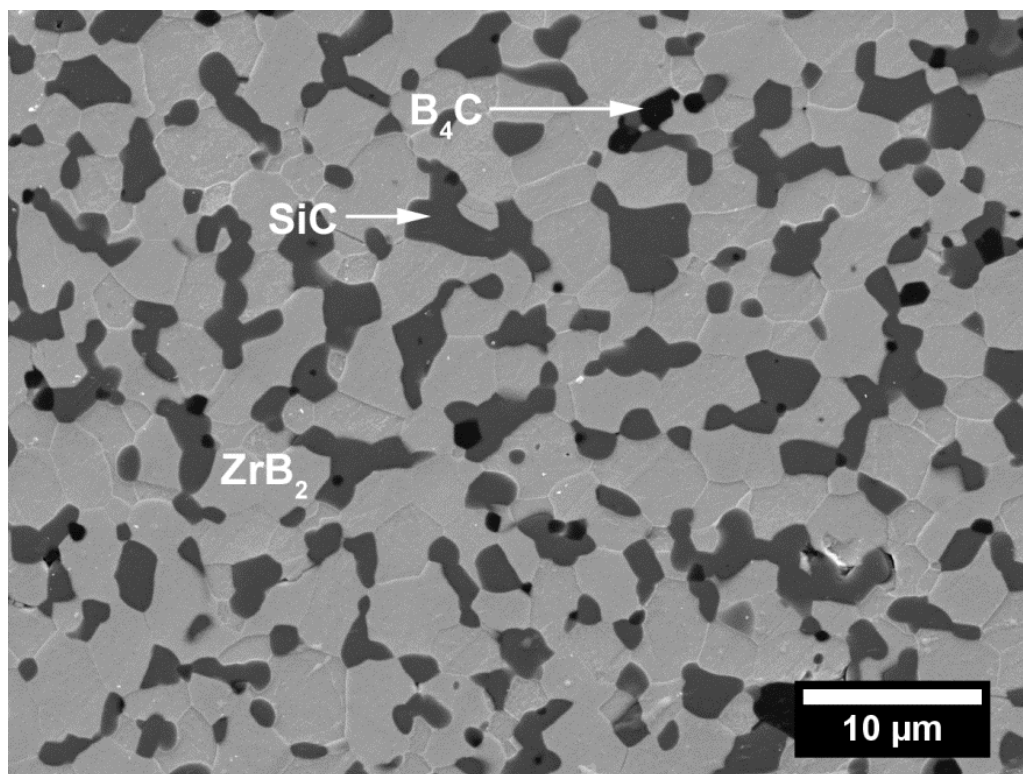


Figure 24. SEM image of a polished and chemically etched cross-section of $\text{ZrB}_2\text{-30SiC}$.

As shown in Figure 25, SEM analysis revealed the presence of microcracks in the ZrB_2 matrix. The maximum SiC cluster size that was observed was $58.9\ \mu\text{m}$, which is well above the microcracking threshold for $\text{ZrB}_2\text{-SiC}$ of $11.5\ \mu\text{m}$ reported by Watts. The microcracks observed in the present study were typically several microns in lengths, originating from SiC grains or clusters. The microcracks appear to either link up with other microcracks, or terminate in the ZrB_2 matrix, shown by the arrows in Figure 25. Thus, the matrix microcracking is a result of the large SiC clusters present in the microstructure.

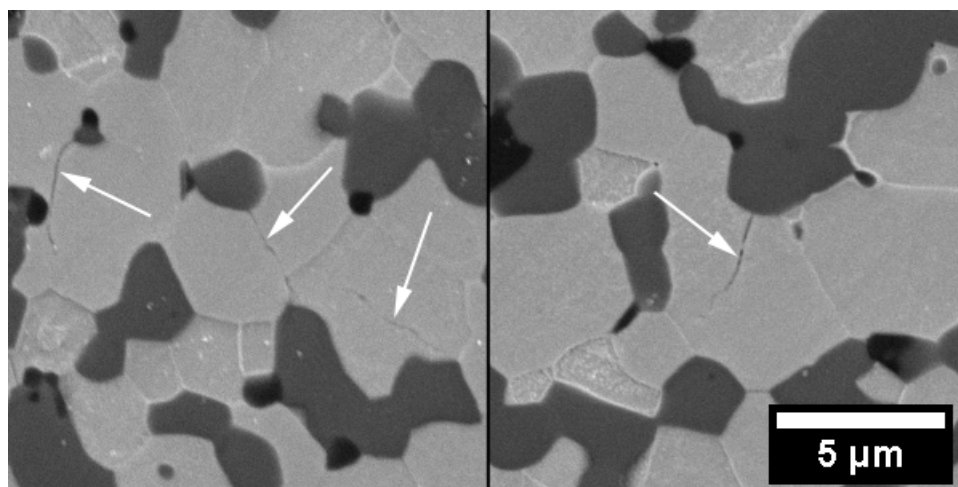


Figure 25. SEM images of chemically etched cross sections of $\text{ZrB}_2\text{-30SiC}$ with arrows showing microcracking.

Measured values for the elastic modulus, flexure strength, and fracture toughness from room temperature to 1600°C are included in Table 14. All of the specimens exhibited linear-elastic behavior to failure, and no creep was observed in the bars following fracture at the elevated temperatures. Figure 26 summarizes the flexural strength as a function of test temperature. Based on the observed trends, the discussion below is divided into temperature regimes of similar behavior.

Table 14. Elevated temperature mechanical properties of ZrB₂ - 30 vol% SiC. Number of samples tested given in parenthesis.

Temperature (°C)	Strength (MPa)	Modulus (GPa)	Toughness (MPa·m ^{1/2})
RT	682 ± 98 (9)	513 ± 24	3.6 ± 0.7 (8)
800	754 ± 99 (9)	432 ± 17	4.8 ± 0.2 (3)
1000	726 ± 68 (10)	408 ± 26	4.5 ± 0.2 (4)
1200	521 ± 107 (10)	326 ± 66	3.9 ± 0.2 (4)
1400	439 ± 41 (8)	247 ± 17	3.8 ± 0.2 (4)
1500	359 ± 23 (5)	209 ± 21	-
1600	384 ± 42 (5)	110 ± 14	3.3 ± 0.2 (5)

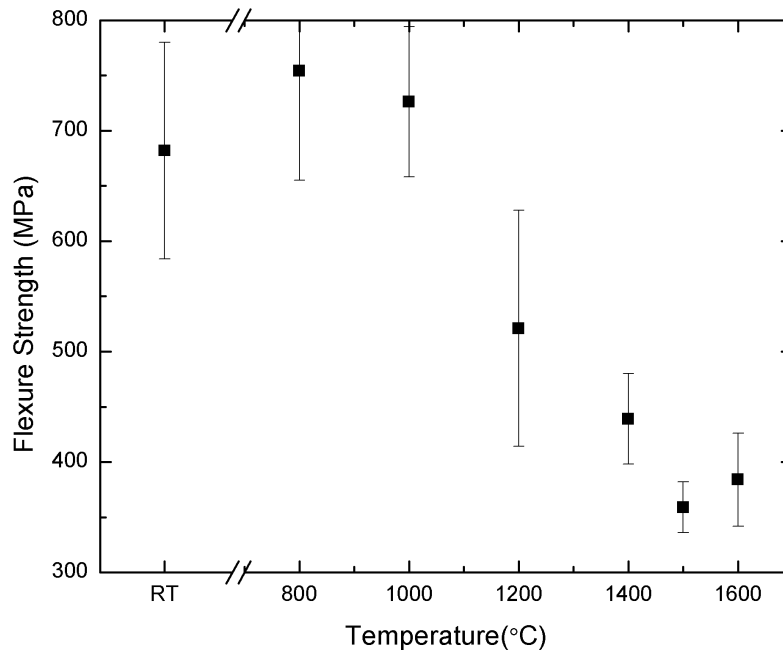


Figure 26. Four-point flexure strength of ZrB₂-30SiC tested in air atmosphere as a function of temperature.

The average strength increased from ~680 MPa at room temperature to ~750 MPa at 800°C. An increase in strength from room temperature to 1000°C or 1200 °C has been previously observed in ZrB₂ and HfB₂ based composites. Figure 27a shows that the tensile surface of the bar tested at 800°C was covered by a dense oxide layer ~3.2 μm thick consisting of ZrO₂+ZrB₂+SiC. The formation of this dense oxide layer may heal flaws present on the surface (i.e. machining damage, microcracking), thus decreasing the flaw size. Kalish *et al.* observed that an increase in the amount of transgranular fracture corresponded to an increase in the strength of ZrB₂. Because the present tests were conducted in an oxidizing environment (i.e., air), any information regarding the type of fracture was lost due to the formation of the oxide scale on the fracture surface, so the amount of transgranular and intragranular fracture could not be determined in the present study. The increase in strength observed between room temperature is due to a decrease in surface flaw size and transition to transgranular fracture.

Above 1000°C, the strength decreased nearly linearly from ~725 MPa at 1000°C to a low of ~360 MPa at 1500°C. At 1000°C the oxide scale (Figure 27b) was ~7 μm thick and appeared to be partially dense. The slight drop in strength between 800°C and 1000°C was likely due to this formation of porosity in the oxide scale. Rhodes *et al.* attributed the decrease in strength to relaxation of thermal stresses that arose during cooling from the processing temperature due to the difference in CTE values between ZrB₂ and SiC. More recently, Watts *et al.* measured residual stresses as a function of temperature and concluded that the stresses were completely relaxed by ~1400°C. Thus, the decrease in strength between 1000°C and 1500°C is consistent with relaxation of thermal stresses.

The strength increased from ~360 MPa at 1500°C to ~380 MPa at 1600°C. Since the residual stress was expected to relax by about 1400°C on heating to the testing temperature, some other mechanism is needed to explain the increase in strength observed between 1500°C and 1600°C. For example, a change in the fracture behavior or the morphology of the oxidation scale could account for the change in strength. A minimum in strength for ZrB₂ was also observed by Rhodes *et al.* to occur around 1400°C, followed by an increase in strength up to 1800 °C. The increase in strength was attributed to plastic flow of the material. Rhodes did not observe the same phenomenon in ZrB₂-20vol% SiC, but did observe a consistent strength between 1400°C and 1800°C. Creep was observed by Rhodes in ZrB₂-20vol% SiC beginning at 1600°C. The strength testing by Rhodes was performed using a constant strain rate. This may have allowed the macroscopic creep effects on the measured strength of the material to counter the benefit of stress relief by plastic flow. The strain rates used in the present study were selected to attain linear elastic fracture at all temperatures as suggested in ASTM C1211-08. This minimizes any creep effects, which would be detrimental to strength, and should allow the stress relief associated with plastic flow to increase the strength in this temperature regime.

Following testing, the bars were cross-sectioned to determine the thickness and morphology of the oxidation scale on the tensile surfaces (Figure 27). At 800°C and 1000°C, a B₂O₃ glassy layer was observed on the surfaces of the samples with a ZrO₂+ZrB₂+SiC layer beneath the outer B₂O₃ layer. The total thickness of the oxide scale at 800°C and 1000°C was ~3.2 μm and ~7.3 μm, respectively. B₂O₃ is soluble in water, thus some of the B₂O₃ dissolved during preparation of the cross-sections obfuscating the measurement of the oxide scale thickness at these temperatures. The oxide scale at 800°C is observed to be dense with porosity developing in the oxide scale at 1000°C.

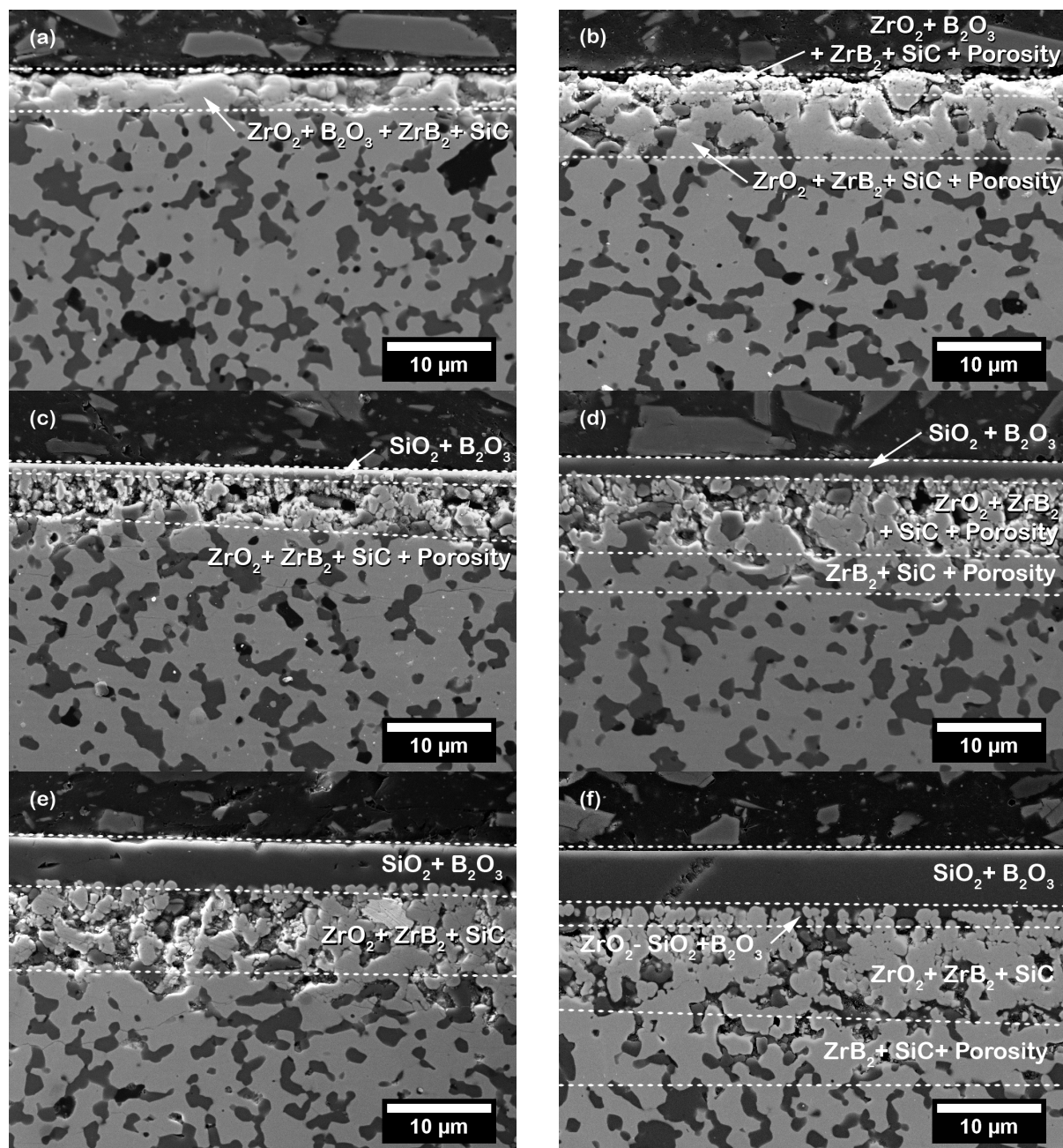


Figure 27. Cross sectional SEM images of the tensile surface of test bars of $\text{ZrB}_2\text{-30SiC}$ after four-point flexure testing at various temperatures in air atmosphere: (a) 800°C; (b) 1000°C; (c) 1200°C; (d) 1400°C; (e) 1500°C; (f) 1600°C.

At 1200°C (Figure 27c), an outer glassy layer that was about 1.3 μm thick was observed on the surface. The outer layer presumably contained SiO_2 and B_2O_3 . Beneath the outer scale was a partially oxidized layer $\sim 5.0 \mu\text{m}$ thick. The partially oxidized layer consisted of ZrO_2 along with partially oxidized ZrB_2 and SiC grains and some porosity. The outer scale grew to $\sim 2.2 \mu\text{m}$ thick at 1400°C and $\sim 4.8 \mu\text{m}$ thick at 1500°C (Figure 27d and e). In addition, the glassy phase partially penetrated into the partially oxidized layer. It can also be seen that partially oxidized SiC grains were present in the ZrO_2 layer at these temperatures, likely due to their large size and

the relatively short time at temperature (10 minutes). At some test conditions, a relatively thin ($\sim 5.0\text{ }\mu\text{m}$ to $8.8\text{ }\mu\text{m}$) but pronounced ZrO_2 layer was observed between the outer glassy layer and the partially oxidized layer. The thickness of the partially oxidized layer increased to $\sim 7.2\text{ }\mu\text{m}$ after testing at 1400°C and $\sim 8.8\text{ }\mu\text{m}$ after oxidation at 1500°C . At these temperatures, the formation of a SiC depleted zone was observed due to the active oxidation of SiC grains. SiC depletion by active oxidation resulted in the formation of porosity in the partially oxidized layer.

The oxidation scale microstructure at 1600°C (Figure 27f) was similar to that observed at 1400°C and 1500°C . The major difference at 1600°C was near full penetration of the glassy phase into the ZrO_2 layer. Additionally, the ZrO_2 layer at 1600°C appears to have a higher density, suggesting that the ZrO_2 grains formed during oxidation had begun to sinter at 1600°C . A number of ZrO_2 islands began to form across the surface at 1500°C . At 1600°C , the ZrO_2 islands on the oxidized surface became larger and the glassy phase transitioned from a smooth to a reticulated coating. The average thickness of the outer glassy scale was $\sim 5.6\text{ }\mu\text{m}$ after testing at 1600°C , with the ZrO_2 and partially oxidized layers having a thickness of $\sim 9.7\text{ }\mu\text{m}$. The structure of the oxidation scales resembled those presented by Rezaie *et al.*, albeit for lower temperatures due to the shorter time at temperature (~ 10 minutes) compared to those presented by Rezaie for longer times (30 minutes). The oxide scale began to lose its effectiveness as a protective coating above 1500°C .

The elastic modulus of $\text{ZrB}_2\text{-SiC}$ decreased as temperature increased (Figure 28). The elastic modulus was 513 GPa at room temperature, which is similar to the values reported by Rezaie *et al.* (503-516 GPa), Zhu *et al.* (509-520 GPa), and Zhang *et al.* (511 GPa). The modulus decreased to 432 GPa at 800°C . Between 1000°C and 1500°C , the elastic modulus decreased from 408 GPa to 209 GPa in a trend that appeared to be linear with temperature. The modulus decreased more rapidly above 1500°C , decreasing to 110 GPa at 1600°C . The change in slope of the trend lines for temperatures from RT to 1000°C and 1000°C to 1500°C may be the result of oxidation. Similar temperature dependencies for modulus and strength have been observed for other oxide and non-oxide ceramics. Wachtman *et al.* found that the elastic modulus of polycrystalline ceramics displayed a gradual linear decrease with increasing temperature in a low temperature range followed by a more rapid, non-linear decrease at higher temperatures. Zhu *et al.* found a similar trend in ZrB_2 , with a slow, linear decrease up to $\sim 1200^\circ\text{C}$ followed by a more rapid decrease above this temperature. Rhodes *et al.* observed a similar trend in the $\text{ZrB}_2\text{-20 vol\% SiC}$ system, where the modulus decreased slowly from 530 GPa at room temperature to 446 GPa at 1400°C , then experienced a rapid decrease to 1600°C to 110 GPa. This rapid decrease in modulus at elevated temperatures has been attributed primarily to grain boundary sliding and diffusional creep. Talmy *et al.* found that grain boundary sliding of SiC was the controlling creep mechanism in $\text{ZrB}_2\text{-SiC}$ ceramics in air. Talmy concluded that increasing the size of the SiC particles in $\text{ZrB}_2\text{-50vol\% SiC}$ from $2\text{ }\mu\text{m}$ to $10\text{ }\mu\text{m}$ increased the creep activation energy from 209 kJ/mol to 511 kJ/mol, which also decreased the amount of creep observed. Further, increasing the amount of SiC ($2\text{ }\mu\text{m}$ particle size) present in the ZrB_2 from 0 vol% to 50 vol% increased the creep activation energy from 130 kJ/mol to 511 kJ/mol, increasing the amount of creep observed as SiC content increased. The material produced by Rhodes had ZrB_2 and SiC grain sizes of $\sim 8\text{ }\mu\text{m}$ and $\sim 4\text{ }\mu\text{m}$. The larger grain size and reduced SiC content of the Rhodes material, compared to the present material, may explain why Rhodes observed more retention of the elastic modulus to higher temperature. These results suggest that increasing the ZrB_2 and SiC grain sizes should increase the stiffness of the material at elevated temperatures.

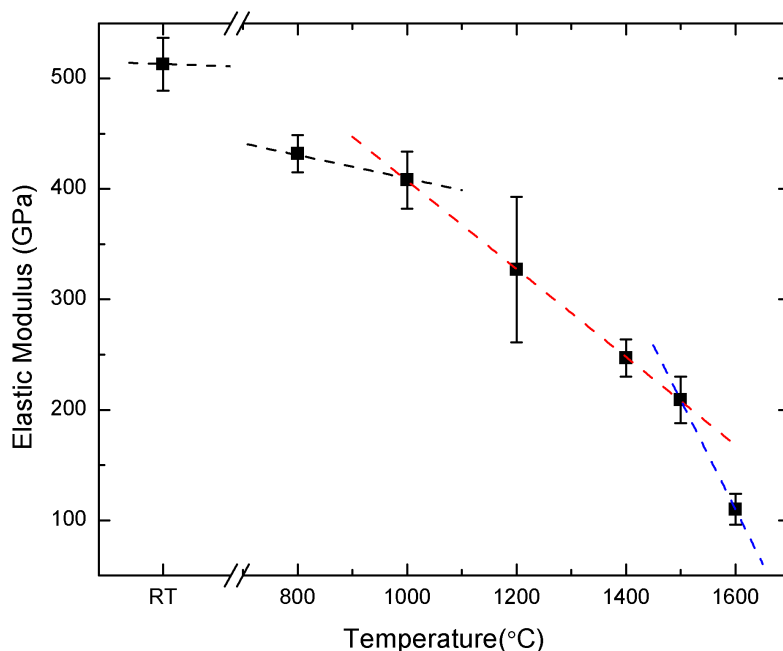


Figure 28. Elastic modulus of ZrB₂-30SiC tested in air atmosphere as a function of temperature. Dashed lines show the linear trend for the three modulus regimes.

The fracture toughness as a function of temperature is shown in Figure 29. At room temperature, the fracture toughness was $3.6 \pm 0.7 \text{ MPa}\cdot\text{m}^{1/2}$, which was considerably less than values ranging from $4.6 \text{ MPa}\cdot\text{m}^{1/2}$ to $5.5 \text{ MPa}\cdot\text{m}^{1/2}$ previously measured for ZrB₂ containing 30 vol% SiC. The lower fracture toughness may be due to the presence of microcracks, which has been shown to decrease toughness in previous studies. In contrast to the spontaneous microcracking observed in the present ZrB₂-SiC, stress induced microcracking can improve the fracture toughness of ceramics by shielding the crack tip and dissipating the fracture energy during crack propagation. However, pre-existing microcracks, such as the spontaneous microcracks formed by thermal expansion mismatch in the present ZrB₂-SiC, do not contribute to crack tip shielding. Rose *et al.* proposed that spontaneous microcracks reduce the fracture toughness by two mechanisms: 1) reducing the initial modulus; and 2) linking with the main crack during fracture. Therefore, the room temperature fracture toughness of the ceramics examined in the present study appears to be lower than expected based on the presence of spontaneous microcracks.

The room temperature values for strength and toughness were $682 \pm 98 \text{ MPa}$ and $3.6 \pm 0.7 \text{ MPa}\cdot\text{m}^{1/2}$. Both were lower than expected from previous studies of ZrB₂-SiC due to spontaneous microcracking. The critical flaw size was predicted for the ZrB₂-30 vol% SiC produced in this study using the Griffith criteria and a Y parameter of 1.28 for a semi-elliptical surface flaw. For room temperature, the predicted critical flaw size was $\sim 34 \text{ }\mu\text{m}$. Repeating the calculation for the elevated temperatures resulted in critical flaw size predictions ranging from $\sim 34 \text{ }\mu\text{m}$ at room temperature to $\sim 90 \text{ }\mu\text{m}$ at 1400°C and 1600°C . The predicted flaw sizes were larger than the average SiC grain size ($1.9 \text{ }\mu\text{m}$), B₄C grain size ($1.1 \text{ }\mu\text{m}$) and B₄C cluster size ($14.4 \text{ }\mu\text{m}$ max) at all temperatures. In addition, the oxide scale thicknesses were less than the predicted critical flaw size for all temperatures. The sizes of the largest SiC clusters (~ 32 to $59 \text{ }\mu\text{m}$ for the largest 0.1% of SiC clusters) fell within the range of critical flaw sizes up to 1000°C . Above 1000°C , the predicted critical flaw size became larger than the largest SiC clusters. This

could mean that the type of critical flaw has changed, which could also mean that the stress intensity factor of 1.28 is no longer valid. For example, a stress intensity factor of $Y = \pi^{1/2}$ (small central, double ended through crack) brings the predicted critical flaw size into the range the largest SiC clusters. Another possibility is that a larger flaw forms at this higher temperature. For example, oxidation damage could produce larger flaws. Another possibility is that thermal strain on heating above 1000°C provides enough energy to drive the growth of cracks already present in the microstructure. Above 1400°C, where thermal stresses have been shown to relax, thermal strain may not be present and thus may not be driving crack growth.

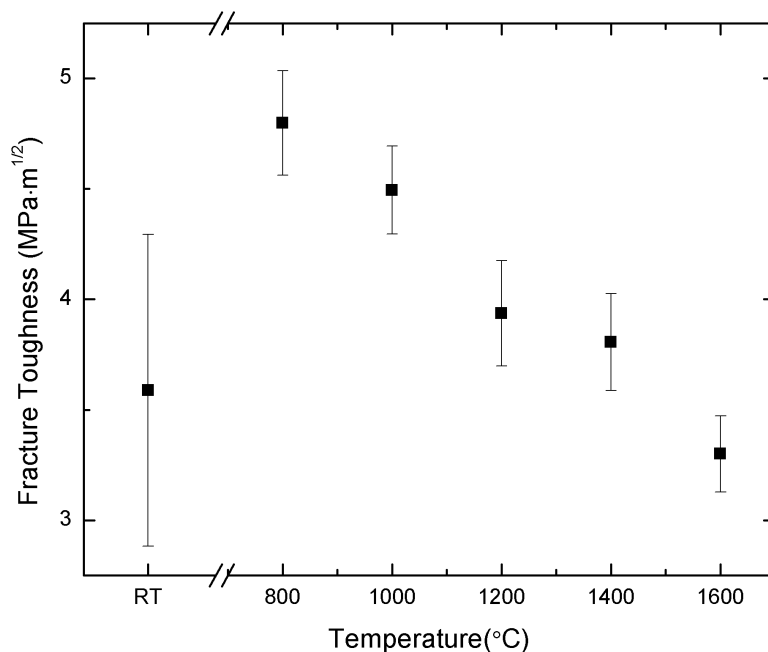


Figure 29. Chevron notch beam, in four point flexure, fracture toughness of ZrB₂-30SiC tested in air as a function of temperature.

To search for strength-limiting flaws for materials tested at elevated temperatures, fragments of the specimens tested at elevated temperatures were fractured in 3-point bending at room temperature, using a support span of 20 mm. Figure 30 shows examples of flaws found in specimens fractured at room temperature after exposure to temperatures of 800°C, 1000°C, 1400°C, and 1600°C. Analysis of the fracture surfaces (ASTM C1322-05b) revealed the critical flaw to be SiC agglomerates from room temperature up to 1000°C. These flaws were typically surface, or near surface, flaws exhibiting circular or semicircular morphologies. At 1200°C and above, oxidation damage was determined to be the critical flaw. The failure origins were characterized by regions of increased penetration of the oxide scale into the bulk material. These regions of increased oxidation damage showed semicircular or long semicircular surface flaw morphologies. The critical flaw sizes calculated from the measured fracture toughness and strength values using a Y parameter of 1.99 (long semicircular surface flaws) were consistent with the depth of oxidation damage that was observed. For example, at 1400°C calculated critical flaw size is $18.9 \pm 2.0 \mu\text{m}$, similar to the measured total oxide scale thickness of $16.7 \pm 2.1 \mu\text{m}$ observed in Figure 27d. Finally, the proposed regimes of behavior are summarized in Figure 31.

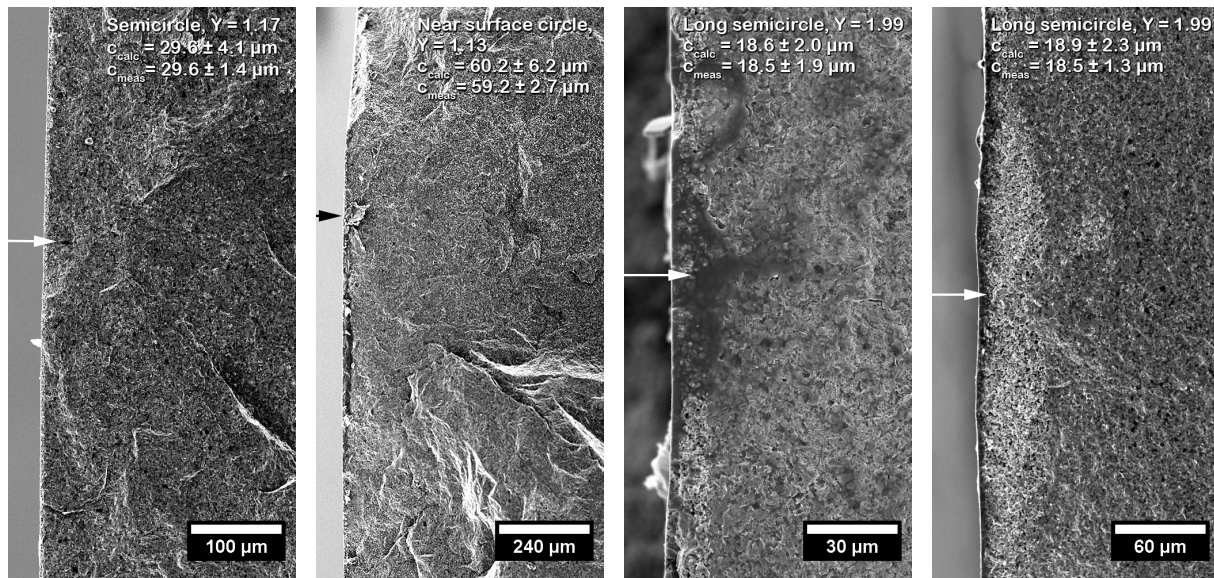


Figure 30. SEM images of the fracture surfaces of a) 800°C, b) 1000°C, c) 1400°C, and d) 1600 test bar fragments broken at room temperature in 3-point flexure. The failure origin is marked by the arrow, and the calculated and measured flaw size for each specimen is given.

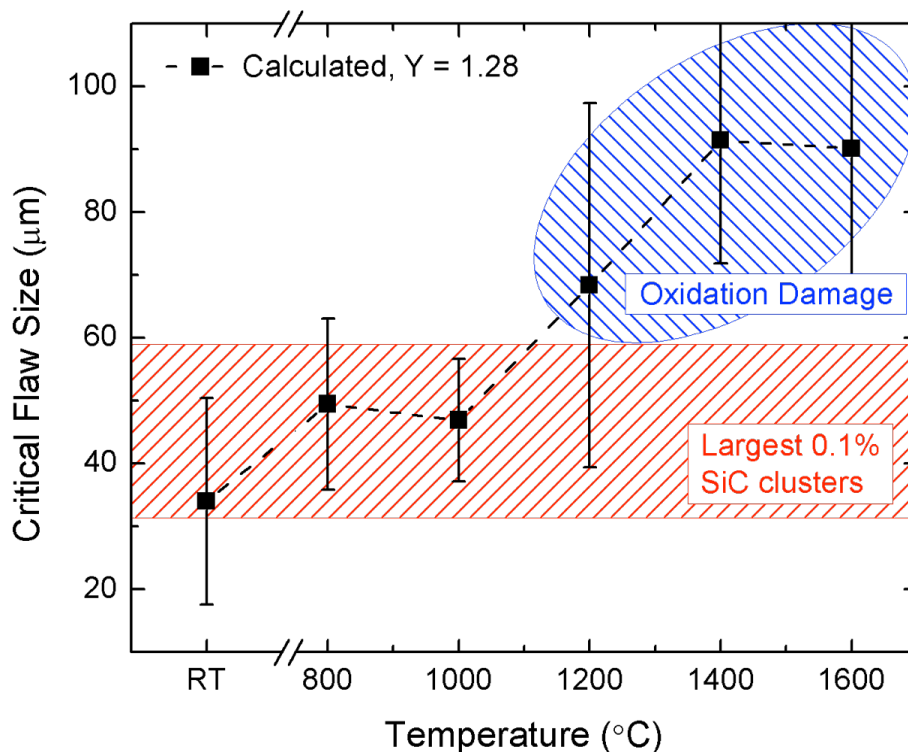


Figure 31. Schematic showing the strength-limiting flaws for ZrB₂-SiC tested in air.

Personnel Supported

Table 15. Personnel supported on AFOSR contract FA9550-09-1-0168.

Name	Title/Role	Level of Support
Dr. Bill Fahrenholtz	Co-PI	1 mo. summer salary
Dr. Greg Hilmas	Co-PI	1 mo. summer salary
Jeremy Watts	Grad. research assist., residual stress	50% time GRA
Matt Thompson	Grad. research assist., thermal properties	50% time GRA
Eric Neuman	Grad. research assist., mechanical properties	50% time GRA
Devon McClane	Grad. research assist., thermal properties	50% time GRA
Derek Guenther	Undergraduate, hot pressing	Part time in 2013
John Tomaszewski	Undergraduate, sample prep, testing	Part time in 2012-13
Daniel Felman	Undergraduate, processing	Part time in 2012
Lucas Showalter	Undergraduate, processing, testing	Part time 2011-12
Cassandra Coley	Undergraduate, processing, sample prep	Part time 2011
Stephen Edgar	Undergraduate, processing, sample prep	Part time 2011
Derek King	Undergraduate, sample prep, testing	Part time 2010
Ryan Wilkerson	Undergraduate, processing, sample prep	Part time 2009-11
Eric Neuman	Undergraduate, processing, testing	Part time in 2009
David Shahin	Undergraduate, processing	Part time in 2009

Publications and Presentations

Peer-Reviewed Journal Papers

1. E.W. Neuman, G.E. Hilmas, and W.G. Fahrenholtz, "Mechanical Behavior of Zirconium Diboride-Silicon Carbide Ceramics at Elevated Temperature in Air," Journal of the European Ceramic Society, 33(15-16) 2889-2899 (2013).
2. J. Watts, G.E. Hilmas, and W.G. Fahrenholtz, "Mechanical Characterization of Annealed ZrB₂-SiC Composites," Journal of the American Ceramic Society, 96(3) 845-851 (2013).
3. E.W. Neuman, H.J. Brown-Shaklee, J.L. Watts, G.E. Hilmas, and W.G. Fahrenholtz, "Case Study: Building an Ultra-High Temperature Mechanical Testing System," American Ceramic Society Bulletin, 92(1) 36-38 (2013).
4. E.W. Neuman, G.E. Hilmas, and W.G. Fahrenholtz, "Strength of Zirconium Diboride to 2300°C," Journal of the American Ceramic Society, 96(1) 47-50 (2013).
5. M.J. Thompson, W.G. Fahrenholtz, and G.E. Hilmas, "Elevated Temperature Thermal Properties of ZrB₂ with Carbon Additions," Journal of the American Ceramic Society, 95(3) 1077-1085 (2012).
6. W.G. Fahrenholtz and G.E. Hilmas, "Oxidation of Ultra-High Temperature Transition Metal Diboride Ceramics," International Materials Reviews, 57(1) 61-72 (2012).
7. J. Watts, G.E. Hilmas, and W.G. Fahrenholtz, "Mechanical Characterization of ZrB₂-SiC Composites with Varying SiC Particle Sizes," Journal of the American Ceramic Society, 94(12) 4410-4418 (2011).
8. J. Watts, G. Hilmas, W.G. Fahrenholtz, D. Brown, and B. Clausen, "Measurement of Thermal Residual Stresses in ZrB₂-SiC Composites," Journal of the European Ceramic Society, 31(9) 1811-1820 (2011).

9. M.J. Thompson, W.G. Fahrenholtz, and G.E. Hilmas, "Effect of Starting Particle Size and Oxygen Content on the Densification of ZrB_2 ," *Journal of the American Ceramic Society*, 94(2) 429-435 (2011).
10. J. Watts, G.E. Hilmas, W.G. Fahrenholtz, D. Brown, and B. Clausen, "Stress Measurement in ZrB_2 -SiC Ceramics using Raman Spectroscopy and Neutron Diffraction," *Journal of the European Ceramic Society*, 30(11) 2165-2171 (2010).

Theses and Dissertations

1. E.W. Neuman, "Elevated Temperature Mechanical Properties of Zirconium Diboride Based Ceramics," PhD Dissertation, Missouri University of Science and Technology, Rolla, MO, scheduled to defend in December 2013.
2. D. McClane, "Transition Metal Additions to Zirconium Diboride," MS thesis, Missouri University of Science and Technology, Rolla, MO, planning to defend in April 2014.
3. M.J. Thompson, "Densification and Thermal Properties of ZrB_2 -Based Ceramics," PhD Dissertation, Missouri University of Science and Technology, Rolla, MO, Dec. 2011.
4. J. Watts, "Stress Measurement and Development of ZrB_2 -SiC Ceramics," PhD Dissertation, Missouri University of Science and Technology, Rolla, MO, Dec. 2011.

Invited Presentations

1. W.G. Fahrenholtz and G.E. Hilmas, "Processing and Properties of Ceramics for Extreme Environments," Savannah River National Laboratory Director's Colloquium, Savannah River National Laboratory, Aiken, SC, October 10, 2013.
2. W.G. Fahrenholtz and G.E. Hilmas, "Effects of Microstructure and Composition on Thermal Conductivity of Zirconium Diboride," Keynote Presentation, 13th International Conference of the European Ceramic Society, Limoges, France, June 23-27, 2013.
3. W.G. Fahrenholtz and G.E. Hilmas, "Ultra-High Temperature Ceramics for Hypersonic Aerospace Applications, Materials Science and Engineering Department Seminar, Iowa State University, Ames, IA, September 6, 2012.
4. G.E. Hilmas and W.G. Fahrenholtz, "Ultra-High Temperature Thermal and Mechanical Properties of ZrB_2 -Based Ceramics," Ultra-High Temperature Ceramics: Materials for Extreme Environments II, Hernstein, Austria, May 13-18, 2012.
5. W.G. Fahrenholtz and G.E. Hilmas, "Ceramic Materials for Extreme Environments," 6th Annual Military Armor Protection Conference, February 27-29, 2012, Alexandria, VA.
6. W.G. Fahrenholtz and G.E. Hilmas, "Mechanical and Thermal Properties of Zirconium Diboride Based Ceramics," Composites at Lake Louise 2011, Lake Louise, Alberta, Canada, October 31-November 4, 2011.
7. W.G. Fahrenholtz, "Ultra High Temperature Ceramics for Hypersonic Applications," Summer School on Materials and Structures for Hypersonic Flight, University of California at Santa Barbara, August 16, 2011.
8. W.G. Fahrenholtz and G.E. Hilmas, "UHTC Research at Missouri S&T: Summary of Recent Progress," NASA Ames Research Center, March 31, 2011.
9. W.G. Fahrenholtz and G.E. Hilmas, "Thermal Behavior of ZrB_2 -Based Ultra-High Temperature Ceramics," Institute for Metal Research-Shenyang National Laboratory, Shenyang, China, August 12, 2010.

10. W.G. Fahrenholtz and G.E. Hilmas, "ZrB₂-Based Ceramics for Ultra-High Temperature Applications," CIMTEC 2010: 12th International Ceramics Congress, Montecatini, Italy, June 5-12, 2010.
11. W.G. Fahrenholtz and G.E. Hilmas, "Ultra-High Temperature Ceramics for Aerospace Applications," Materials Engineering Seminar, Purdue University, November 23, 2009, West Lafayette, IN.
12. W.G. Fahrenholtz and G.E. Hilmas, "Oxidation of Zirconium Diboride Based Ultra-High Temperature Ceramics," Materials Science and Technology 2009 Conference and Exhibition, October 25-29, 2009, Pittsburgh, PA.

Contributed Presentations

1. E.W. Neuman, G.E. Hilmas, and W.G. Fahrenholtz, "Ultra High Temperature Mechanical Testing of ZrB₂-Based Ceramics," National Space and Missile Materials Symposium, Bellevue, WA, June 24-27, 2013.
2. E.W. Neuman, G.E. Hilmas, and W.G. Fahrenholtz, "Ultra high temperature mechanical testing of ZrB₂ based ceramics," 13th International Conference of the European Ceramic Society, Limoges, France, June 23-27, 2013.
3. D. McClane, W.G. Fahrenholtz, and G.E. Hilmas, "Thermal Properties of Zirconium Diboride With Transition Metal Additions," The 10th Pacific Rim Conference on Ceramic and Glass Technology, June 2-7, 2013, San Diego, CA.
4. E.W. Neuman, G.E. Hilmas, and W.G. Fahrenholtz, "Ultra-High Temperature Mechanical Testing of ZrB₂-Based Ceramics," National Space and Missile Materials Symposium, Tampa, FL, June 25-28, 2012.
5. E.W. Neuman, G.E. Hilmas, and W.G. Fahrenholtz, "Ultra-High Temperature Mechanical Testing Methodology of ZrB₂-Based Ceramics," Ultra-High Temperature Ceramics: Materials for Extreme Environments II, Hernstein, Austria, May 13-18, 2012 (poster presentation).
6. M.J. Thompson, W.G. Fahrenholtz, and G.E. Hilmas, "Thermal Properties of ZrB₂-TiB₂ Solid Solutions," 36th International Conference on Advanced Ceramics and Composites, January 22-27, 2012, Daytona Beach, FL
7. E.W. Neuman, G.E. Hilmas, and W.G. Fahrenholtz, "Mechanical Properties and Characterization of a Heat-Treated ZrB₂-SiC Composite," 36th International Conference on Advanced Ceramics and Composites, January 22-27, 2012, Daytona Beach, FL
8. J. Watts, G.E. Hilmas, and W.G. Fahrenholtz, "Mechanical Behavior of ZrB₂-SiC Particulate Composites With Varying SiC Particle Sizes," 36th International Conference on Advanced Ceramics and Composites, January 22-27, 2012, Daytona Beach, FL
9. J. Watts, G.E. Hilmas, and W.G. Fahrenholtz, "Stress Measurement in ZrB₂-SiC Ultra-High Temperature Ceramics," PACRIM 9, July 10-14, 2011, Cairns, Australia.
10. M.J. Thompson, G.E. Hilmas, and W.G. Fahrenholtz, "Thermal Properties of ZrB₂ Containing Carbon, Boron Carbide, and Titanium Diboride," National Space and Missile Materials Symposium, June 26-30, 2011, Madison, WI.
11. E.W. Neuman, W.G. Fahrenholtz, and G.E. Hilmas, "Thermomechanical Properties and Characterization of Heat Treated ZrB₂-SiC Composites," National Space and Missile Materials Symposium, June 26-30, 2011, Madison, WI.

12. J. Watts, G. Hilmas, and W.G. Fahrenholtz, "Stress Measurement of $\text{Zr}^{11}\text{B}_2/\text{SiC}$ Composites using Neutron Diffraction and Raman Spectroscopy," 35th International Conference on Advanced Ceramics and Composites, January 24-28, 2011, Daytona Beach, FL.
13. E.W. Neuman, G.E. Hilmas, and W.G. Fahrenholtz, "Thermomechanical Properties and Characterization of Heat Treated $\text{ZrB}_2\text{-SiC}$ Composites," 35th International Conference on Advanced Ceramics and Composites, January 24-28, 2011, Daytona Beach, FL.
14. M. Thompson, W.G. Fahrenholtz, and G.E. Hilmas, "Additive Effects on the Thermal Properties of ZrB_2 ," 35th International Conference on Advanced Ceramics and Composites, January 24-28, 2011, Daytona Beach, FL.
15. M. Thompson, W.G. Fahrenholtz, and G.E. Hilmas, "Effect of Heating Rate on the Densification of ZrB_2 ," 35th International Conference on Advanced Ceramics and Composites, January 24-28, 2011, Daytona Beach, FL.
16. M.J. Thompson, W.G. Fahrenholtz, and G.E. Hilmas, "High Temperature Thermal Properties of ZrB_2 ," National Space and Missile Materials Symposium, June 26-July 2, 2010, Phoenix, AZ.
17. M.J. Thompson, W.G. Fahrenholtz, and G.E. Hilmas, "Effect of Heating Rate on the Densification of ZrB_2 ," 34th International Conference on Advanced Ceramics and Composites, January 25-29, 2010, Daytona Beach, FL.
18. J. Watts, G.E. Hilmas and W.G. Fahrenholtz, "Stress measurement in annealed $\text{ZrB}_2\text{-SiC}$ composites," 34th International Conference on Advanced Ceramics and Composites, January 25-29, 2010, Daytona Beach, FL.
19. J. Watts, G. Hilmas, and W. Fahrenholtz, "Stress Measurements in $\text{ZrB}_2\text{-SiC}$ Composites Using Neutron Diffraction," The 5th International Conference on Mechanical Stress Evaluation by Neutrons and Synchrotron Radiation, November 10-12, 2009, Mito, Japan.
20. J. Watts, G.E. Hilmas, and W.G. Fahrenholtz, "Modeling and Measuring Residual Stresses in $\text{ZrB}_2\text{-SiC}$ Ceramics," AFOSR Workshop on Aerospace Materials for Extreme Environments, August 3-5, 2009, St. Louis, MO.
21. M.J. Thompson, W.G. Fahrenholtz, and G.E. Hilmas, "Densification and Microstructure of ZrB_2 ," AFOSR Workshop on Aerospace Materials for Extreme Environments, August 3-5, 2009, St. Louis, MO.
22. J. Watts, M.P. Teague, G.E. Hilmas, W.G. Fahrenholtz, "Stress Measurement in $\text{ZrB}_2\text{-SiC}$ Composites Via Neutron Diffraction," 33rd International Conference on Advanced Ceramics and Composites, January 18-23, 2009, Daytona Beach, FL.
23. M.J. Thompson, W.G. Fahrenholtz, G.E. Hilmas, and M. Cinibulk, "Effects of Densification Method and Grain Size on Mechanical Properties of Zirconium Diboride," 33rd International Conference on Advanced Ceramics and Composites, January 18-23, 2009, Daytona Beach, FL.

Interactions/Transitions

1. Graduate student Eric Neuman spent one month at Imperial College in London during late summer of 2012. During his visit, Eric collaborated with Professor W.E. Lee and Dr. Doni Daniel. The focus of the interaction with Imperial College was to perform high resolution transmission electron microscopy on diboride ceramic specimens produced by Eric as part of his research. The effort led to insight into the composition of grain

boundary phases and the presence of impurities that have been used in the dissertation research and subsequent manuscripts.

2. The project team had significant interactions with the Air Force Research Laboratory at Wright-Patterson Air Force Base. In particular, the team worked with Dr. Mike Cinibulk throughout the course of the project. Among the interactions were coordinating the use of spark plasma sintering equipment, discussing test results, and analyzing oxidation data in collaboration with Dr. Cinibulk and other researchers from AFRL.
3. The project team collaborated with Dr. Heikki Helava from Helava Systems as part of the project. The nature of the interactions are subject to a non-disclosure agreement, but can be disclosed to and discussed with government personnel upon request.
4. We have an on-going collaboration with Dr. Jochen Marschall at SRI International related to ultra-high temperature ceramics. In the past year, graduate student Matt Thompson has been working with Joe and his post-doc Luning Zhang to study the effect of carbon content on the thermal properties of ZrB₂-based ceramics. Matt prepared a series of ZrB₂ based ceramics with a range of carbon contents that were analyzed by both laboratories. The intent is for each group to prepare an independent manuscript on the measurements that they performed and then work on a joint manuscript after the first manuscripts are drafted.
5. We have been in contact with Dr. Arun Shukla from the University of Delaware about a potential future collaboration. Dr. Shukla has an AFOSR grant through the mechanics program and was directed to our group by one of his collaborators at AFRL. Dr. Shukla uses shock loading and dynamic tests to study the mechanical response of materials. We are planning to prepare a series of ZrB₂-based specimens for him to study. After the initial set of samples, he would like for us to prepare some cermet samples for a follow-on study.

Awards

Dr. Bill Fahrenholtz National Institute of Ceramic Engineers Greaves-Walker Award for Lifetime Service, Awarded at Materials Science and Technology 2013, Montreal, Canada, October 27-31, 2013

Missouri S&T Outstanding Teaching Award, 2012-13, to be presented November 18, 2013

Promotion to Curators' Professor effective January 2013

Missouri S&T Faculty Service Award and Faculty Research Award 2010

Missouri S&T Faculty Excellence Award 2009

Dr. Greg Hilmas American Ceramic Society/National Institute of Ceramic Engineers Arthur
L. Friedberg Ceramic Engineering Tutorial and Lecture, at Materials
Science and Technology 2013, Montreal, Canada, October 27-31, 2013

Missouri S&T Outstanding Teaching Awards, 2012-13 2011-12, 2010-11,
2009-10

Promotion to Curators' Professor effective January 2012

Missouri S&T Faculty Research Award 2010

Missouri S&T Faculty Excellence Award 2009

Elected Fellow of the American Ceramic Society, 2009

Appendix A: PhD Dissertation of Jeremy Watts

Jeremy Watts completed his PhD dissertation during this project. His thesis was titled “Stress Measurement and Development of Zirconium Diboride-Silicon Carbide Ceramics.” The thesis is available through the library at Missouri S&T. The four main chapters of the thesis are manuscripts that have been published in technical journals. The citations are:

1. J. Watts, G.E. Hilmas, and W.G. Fahrenholtz, “Mechanical Characterization of Annealed ZrB₂-SiC Composites,” *Journal of the American Ceramic Society*, 96(3) 845-851 (2013).
2. J. Watts, G.E. Hilmas, and W.G. Fahrenholtz, “Mechanical Characterization of ZrB₂-SiC Composites with Varying SiC Particle Sizes,” *Journal of the American Ceramic Society*, 94(12) 4410-4418 (2011).
3. J. Watts, G.E. Hilmas, and W.G. Fahrenholtz, “Mechanical Characterization of ZrB₂-SiC Composites with Varying SiC Particle Sizes,” *Journal of the American Ceramic Society*, 94(12) 4410-4418 (2011).
4. J. Watts, G.E. Hilmas, W.G. Fahrenholtz, D. Brown, and B. Clausen, “Stress Measurement in ZrB₂-SiC Ceramics using Raman Spectroscopy and Neutron Diffraction,” *Journal of the European Ceramic Society*, 30(11) 2165-2171 (2010).

Abstract

Research presented in this dissertation focused on the production of ZrB₂-SiC composites and their characterization; in particular their mechanical properties and thermally generated residual stresses. Thermally generated stresses were measured using Raman spectroscopy as well as both neutron and x-ray diffraction. For 70 vol% ZrB₂- 30 vol% SiC composites, neutron diffraction revealed that the SiC phase was under ~880 MPa compressive stress and the ZrB₂ phase was under ~450 MPa tension at room temperature. It was also discovered that stresses began to accumulate at ~1400°C upon cooling from the processing temperature (1900°C to 2000°C). Raman spectroscopy and x-ray diffraction agreed well with one another and showed the stresses in the SiC phase on the surface of the samples to be ~350 MPa; lower than that in the bulk as measured by neutron diffraction. It has also been shown that annealing composites at temperatures below 1400°C, particularly under pressure, can partially relieve these stresses leading to increases in mechanical strength of as much as 30%.

The role of the particle size of the SiC phase was also investigated. For SiC particle sizes smaller than 11.5 μm, the failure strengths of the composites followed a $c^{-1/2}$ relationship as predicted by Griffith. Above that particle size however, strength, modulus, and hardness all decreased rapidly. It was discovered that for SiC particle sizes larger than 11.5 μm microcracking occurred resulting in the decrease of the measured mechanical properties.

Appendix B: PhD Dissertation of Matthew Thompson

Matthew J. Thompson completed his PhD dissertation during this project. The thesis was titled “Densification and Thermal Properties of Zirconium Diboride Based Ceramics”. It is available through the library at Missouri S&T. The four main chapters of the thesis are in manuscript form. Two of these manuscripts have been published at this time. The citations are:

1. M.J. Thompson, W.G. Fahrenholtz, and G.E. Hilmas, “Elevated Temperature Thermal Properties of ZrB_2 with Carbon Additions,” *Journal of the American Ceramic Society*, 95(3) 1077-1085 (2012).
2. M.J. Thompson, W.G. Fahrenholtz, and G.E. Hilmas, “Effect of Starting Particle Size and Oxygen Content on the Densification of ZrB_2 ,” *Journal of the American Ceramic Society*, 94(2) 429-435 (2011).

Abstract

The research presented in this dissertation focuses on the processing and thermomechanical properties of ZrB_2 based ceramics. The overall goal was to improve the understanding of thermal and mechanical properties based on processing conditions and additives to ZrB_2 . To achieve this, the relationships among microstructure and thermal, mechanical properties were analyzed for ZrB_2 ceramics that were densified by different methods, with varying amounts of carbon or B_4C , or with TiB_2 additions.

Four main areas were investigated in this dissertation. The first showed how decreased processing times, regardless of densification method, improved mechanical strength to >500 MPa. This study also revealed that lower oxygen impurity contents led to less grain coarsening. The second investigated the effect of heating rate during hot pressing and spark plasma sintering on the mechanical strength. Higher heating rates limited the grain size distribution, which resulted in strengths above 600 MPa. However, the decreased processing times, led to retention of ZrO_2 , which decreased the thermal conductivity. The third study revealed that carbon additions interacted with ZrO_2 and WC impurities introduced during powder processing to form $(\text{Zr,W})\text{C}$, which led higher thermal conductivity than ZrB_2 with no carbon added. The last area examined the effect of solid solution additions on the electron and phonon contributions to thermal conductivity. The formation of solid solutions decreased thermal conductivity to <60 W/m•K compared to 93 W/m•K for nominally pure ZrB_2 .

Taken as a whole, this research adds insight into the fundamental aspects of microstructure and composition that control the thermal and mechanical properties of ZrB_2 . Processing parameters such as densification method and heating rate control microstructure development including removal of oxides, grain size, and second phases. Additives like carbon or TiB_2 affect phases present and thermal transport mechanisms. These changes impact thermal and mechanical properties, which control the performance of ZrB_2 based ceramics.

Appendix C: PhD Dissertation of Eric Neuman

Eric W. Neuman will complete his PhD dissertation during the spring of 2014. His research was completed during this project, but his defense date was scheduled after the end of the project. His thesis will be available in the Missouri S&T library when it is completed. The main chapters of his dissertation will be manuscripts. Two of the manuscripts have already been published and are listed as numbers 1) and 2) below. Three additional manuscripts listed as numbers 3), 4), and 5) below will be submitted for publication when they are completed.

1. E.W. Neuman, G.E. Hilmas, and W.G. Fahrenholtz, "Mechanical Behavior of Zirconium Diboride-Silicon Carbide Ceramics at Elevated Temperature in Air," *Journal of the European Ceramic Society*, 33(15-16) 2889-2899 (2013).
2. E.W. Neuman, G.E. Hilmas, and W.G. Fahrenholtz, "Strength of Zirconium Diboride to 2300°C," *Journal of the American Ceramic Society*, 96(1) 47-50 (2013).
3. E.W. Neuman, G.E. Hilmas, and W.G. Fahrenholtz, "Mechanical Behavior of Zirconium Diboride-Silicon Carbide Ceramics up to 2200°C," manuscript in preparation
4. E.W. Neuman, G.E. Hilmas, and W.G. Fahrenholtz, "Elevated Temperature Strength Enhancement of ZrB₂-30 vol% SiC Ceramics by Post-Sintering Thermal Annealing," manuscript in preparation
5. E.W. Neuman, G.E. Hilmas, and W.G. Fahrenholtz, "Ultra-High Temperature Mechanical Behavior of a Zirconium Diboride-Zirconium Carbide Ceramic," manuscript in preparation.

Abstract

Research presented in this dissertation focused on the mechanical behavior of ZrB₂ based ceramic at elevated temperatures. Flexure strength, fracture toughness, and elastic modulus were measured at temperatures up to 2300°C for three compositions: monolithic ZrB₂ (Z); ZrB₂ – 30 vol% SiC – 2 vol% B₄C (ZS); and ZrB₂ – 10 vol% ZrC (ZC). In argon, Z, ZS, and ZC had strengths of 210 (at 2300°C), 260 (at 2200°C), and 295 MPa (at 2300°C), the highest temperatures tested for each composition. Fractography was used extensively to characterize the strength limiting flaws as a function of temperature. Strength of ZS in argon was controlled by the SiC cluster size up to 1800°C, and the formation of B-O-C-N phases that bridged SiC clusters above 2000°C. For ZC, surface flaws introduced during specimen preparation were the source of critical flaws in the material up to 1400°C, sub-critical crack growth of surface flaws between 1600 and 2000°C, and micro void coalescence above 2000°C.

It was also shown that thermal annealing at either 1400, 1500, or 1600°C improves the strength and modulus of ZS at temperatures between 800°C and 1600°C. Heat treatment at 1400°C for 10 hours produced the largest improvement in strength, 430 MPa at 1600°C versus 380 MPa for the as processed material. As a whole, the research pointed to several key microstructural features currently limiting the mechanical properties at the highest temperatures. In particular, removal of unfavorable secondary phases, and improved control over microstructure, should be promising methods to improve the elevated temperature properties of ZrB₂ ceramics.

Appendix D: MS thesis of Devon McClane

Devon McClane will complete his MS Thesis during the spring of 2014. The tentative title of his thesis is “Effect of Transition Metal Additions on Thermal Properties of Zirconium Diboride”. His thesis will be available in the Missouri S&T library when it is completed. The main chapters of his dissertation will be manuscripts. One of the manuscripts has been submitted for publication while the other will be submitted for publication when it is completed.

1. D.L. McClane, W.G. Fahrenholtz, and G.E. Hilmas, “Thermal Properties of Zirconium Diboride with Subgroup V, VI, and VII Transition Metal Boride Additions,” manuscript in preparation.
2. D.L. McClane, W.G. Fahrenholtz, and G.E. Hilmas, “Thermal Properties of Zirconium Diboride With Transition Metal Boride Additions,” submitted to the Journal of the American Ceramic Society, November 20, 2013.

Abstract

The research presented in this thesis focuses on the thermal properties of zirconium diboride (ZrB_2) based ceramics. The overall goal was to improve the understanding of how transition metal additives influence thermal transport in ZrB_2 . To achieve this, ZrB_2 with 0.5 wt% carbon, and 3 mol% of a transition metal boride (TMB) was densified via hot-press sintering. The transition metals that were investigated include: yttrium, titanium, hafnium, vanadium, niobium, tantalum, chromium, molybdenum, tungsten, and rhenium. Scanning electron microscopy (SEM) was used to examine microstructures and x-ray diffraction (XRD) was used to ensure that the transition metal additives went into solid solution. Laser flash analysis was used to determine the thermal diffusivity of the compositions according to the Clark and Taylor method. Values ranged from $0.331 \text{ cm}^2/\text{s}$ to $0.105 \text{ cm}^2/\text{s}$ at room temperature and converged around $0.155 \text{ cm}^2/\text{s}$ at higher temperatures. Thermal conductivity was calculated from the measured diffusivity, using temperature-dependent values for density and heat capacity. In general, transition metals that are located farther to the right on the periodic table have a larger influence on thermal conduction. The four point probe van der Pauw method was used to determine electrical resistivity. The electron contribution to thermal conductivity was calculated from the measured resistivity according to the Wiedemann-Franz law using the Sommerfeld Lorenz number. These results revealed that thermal conduction was dominated by the electron contribution for all of the compositions, especially at high temperatures. Additionally, the addition of a TMB to ZrB_2 decreased the electron contribution by a larger percentage than the total thermal conductivity. The phonon contribution to thermal conductivity was calculated by subtracting the electron contribution from the total thermal conductivity. In some cases this resulted in a negative value, indicating that the theoretical Lorenz number is not a good fit for ZrB_2 . Rietveld refinement of XRD data was used to determine the lattice parameters of the compositions. As the Linus Pauling (CN12) metallic radii of the additive decreased, the lattice volume decreased and was placed under a strain. Additional strain appears to exist for TMBs that would normally have a different crystal symmetry than ZrB_2 . It was found that the apparent strain caused by the difference in size of the transition metal that substitutes for Zr in the lattice correlates directly to the decrease in thermal conduction. This research provides insight into how additives and impurities affect thermal transport in ZrB_2 , as well as potentially offering a basis for future modeling of thermal conductivity in ultra-high temperature ceramics.